Galaxy And Mass Assembly (GAMA): improved cosmic growth measurements using multiple tracers of large-scale structure

Chris Blake,[1]⋆ I. K. Baldry,[2] J. Bland-Hawthorn,[3] L. Christodoulou,[4] M. Colless,[5] C. Conselice,[6] S. P. Driver,[7,8] A. M. Hopkins,[9] J. Liske,[10] J. Loveday,[11] P. Norberg,[12] J. A. Peacock,[13] G. B. Poole[14] and A. S. G. Robotham[7,8]

[1]*Centre for Astrophysics & Supercomputing, Swinburne University of Technology, PO Box 218, Hawthorn, VIC 3122, Australia*
[2]*Astrophysics Research Institute, Liverpool John Moores University, IC2, Liverpool Science Park, 146 Brownlow Hill, Liverpool L3 5RF, UK*
[3]*Sydney Institute for Astronomy, School of Physics, University of Sydney, NSW 2006, Australia*
[4]*Institute of Cosmology & Gravitation, Dennis Sciama Building, University of Portsmouth, Portsmouth PO1 3FX, UK*
[5]*Research School of Astronomy and Astrophysics, The Australian National University, Canberra, ACT 2611, Australia*
[6]*School of Physics & Astronomy, University of Nottingham, University Park, Nottingham NG7 2RD, UK*
[7]*International Centre for Radio Astronomy Research (ICRAR), University of Western Australia, Crawley, WA 6009, Australia*
[8]*SUPA, School of Physics and Astronomy, University of St Andrews, North Haugh, St Andrews, KY16 9SS, UK*
[9]*Australian Astronomical Observatory, PO Box 915, North Ryde, NSW 1670, Australia*
[10]*European Southern Observatory, Karl-Schwarzschild-Str. 2, D-85748 Garching, Germany*
[11]*Astronomy Centre, University of Sussex, Falmer, Brighton BN1 9QH, UK*
[12]*Institute for Computational Cosmology, Department of Physics, Durham University, South Road, Durham DH1 3LE, UK*
[13]*Institute for Astronomy, University of Edinburgh, Royal Observatory, Blackford Hill, Edinburgh EH9 3HJ, UK*
[14]*School of Physics, University of Melbourne, Parkville, VIC 3010, Australia*

ABSTRACT

We present the first application of a 'multiple-tracer' redshift-space distortion (RSD) analysis to an observational galaxy sample, using data from the Galaxy and Mass Assembly (GAMA) survey. Our data set is an $r < 19.8$ magnitude-limited sample of 178 579 galaxies covering the redshift interval $z < 0.5$ and area 180 deg^2. We obtain improvements of 10–20 per cent in measurements of the gravitational growth rate compared to a single-tracer analysis, deriving from the correlated sample variance imprinted in the distributions of the overlapping galaxy populations. We present new expressions for the covariances between the auto-power and cross-power spectra of galaxy samples that are valid for a general survey selection function and weighting scheme. We find no evidence for a systematic dependence of the measured growth rate on the galaxy tracer used, justifying the RSD modelling assumptions, and validate our results using mock catalogues from *N*-body simulations. For multiple tracers selected by galaxy colour, we measure normalized growth rates in two independent redshift bins $f\sigma_8(z = 0.18) = 0.36 \pm 0.09$ and $f\sigma_8(z = 0.38) = 0.44 \pm 0.06$, in agreement with standard GR gravity and other galaxy surveys at similar redshifts.

Key words: surveys – cosmological parameters – large-scale structure of Universe.

1 INTRODUCTION

The large-scale structure of the Universe is one of the most valuable probes of the cosmological model, enabling measurements to be performed of the cosmic distance scale and expansion rate, the constituents of the Universe and the gravitational forces which drive the growth of structure with time. In particular, the 'gravitational growth rate' is accessible through the imprint of redshift-space distortion

(RSD) in the pattern of structure. RSD describes the apparent anisotropic clustering induced by the small shifts in galaxy redshifts that result from the correlated peculiar velocities that galaxies possess in addition to the underlying Hubble-flow expansion.

This cosmic structure has been mapped out by a sequence of galaxy redshift surveys such as the 2-degree Field Galaxy Redshift Survey (2dFGRS; Colless et al. 2001), the 6-degree Field Galaxy Survey (6dFGS; Jones et al. 2009), the Sloan Digital Sky Survey (SDSS; York et al. 2000), the WiggleZ Dark Energy Survey (Drinkwater et al. 2010) and the Baryon Oscillation Spectroscopic Survey (BOSS; Dawson et al. 2013). The accuracy of cosmological

⋆ E-mail: cblake@astro.swin.edu.au

measurements is often limited by 'sample variance', the inherent fluctuations between different portions of the Universe. In order to obtain more precise measurements, the scientific progress of galaxy redshift surveys has emphasized mapping ever greater cosmic volumes, often targeting a relatively sparse distribution of a single type of galaxies [with number density $\sim 10^{-4} \, h^3 \, \mathrm{Mpc}^{-3}$, where $h = H_0/(100 \, \mathrm{km \, s^{-1} \, Mpc^{-1}})$ parameterizes Hubble's constant H_0], chosen by considerations of observational efficiency. For example, the WiggleZ Survey obtained the spectra of emission line galaxies (Drinkwater et al. 2010), whereas BOSS has instead focused on luminous red galaxies (Dawson et al. 2013). Although these 'single-tracer' surveys have allowed increasingly precise tests of the cosmological model, recent examples of RSD growth-rate analyses include Blake et al. (2011), Reid et al. (2012), Beutler et al. (2012), Samushia, Percival & Raccanelli (2012), Contreras et al. (2013) and de la Torre et al. (2013), there are a number of potential advantages of multiple-tracer surveys which we explore in this study.

First, surveying multiple populations of galaxies allows the key assumptions needed to extract cosmological measurements to be examined in an empirical way. A fundamental systematic-error test is that our cosmological conclusions should not depend on the galaxy population used to trace the large-scale structure. We flag in particular the importance of modelling the *galaxy bias* which describes how galaxy tracers populate the underlying large-scale structure. When using RSD to measure the growth rate of structure $f = \mathrm{d} \ln \delta_m/\mathrm{d} \ln a$ in terms of the rate of change in amplitude of a density perturbation δ_m with cosmic scale factor a, it is common to assume that the galaxy bias is linear and deterministic, described by a single parameter b which links the galaxy and matter overdensities at position $\boldsymbol{x}$, $\delta_g(\boldsymbol{x}) = b \, \delta_m(\boldsymbol{x})$. In this case, the clustering anisotropy in redshift space, i.e. the difference in the amplitude of galaxy clustering as a function of the angle to the line of sight, only depends on f/b. However, in reality the galaxy bias is non-linear, scale dependent and stochastic (e.g. Dekel & Lahav 1999; Wild et al. 2005; Swanson et al. 2008; Cresswell & Percival 2009; Marin 2011; Marin et al. 2013), and depends on the detailed manner in which galaxies populate dark matter haloes. Comparison of growth-rate measurements based on different galaxy tracers provides a strict test of the modelling assumptions.

Secondly, a number of authors have pointed out that the availability of multiple galaxy tracers across a volume of space allows improved statistical errors in the measurements of certain cosmological parameters (McDonald & Seljak 2009; Seljak 2009; White, Song & Percival 2009; Gil-Marin et al. 2010; Bernstein & Cai 2011; Hamaus, Seljak & Desjacques 2012; Abramo & Leonard 2013). These improvements derive from the fact that, under the assumption of linear galaxy bias, the tracers encode a common sample variance. The simplest example of this effect is to consider the overdensities in two different galaxy populations which trace a single matter overdensity: $\delta_{g,1}(\boldsymbol{x}) = b_1 \, \delta_m(\boldsymbol{x})$, $\delta_{g,2}(\boldsymbol{x}) = b_2 \, \delta_m(\boldsymbol{x})$. Neglecting all other forms of noise, the ratio of these measured galaxy overdensities allows the precise determination of b_2/b_1 independently of the sample variance contained in δ_m.

The next simplest illustration, of particular relevance for our analysis, is to consider measurements of the complex Fourier amplitudes $\tilde{\delta}_{g,1}(\boldsymbol{k})$ and $\tilde{\delta}_{g,2}(\boldsymbol{k})$ of the overdensity of two tracers for the same wavevector $\boldsymbol{k}$, which has some angle to the line of sight whose cosine is denoted by μ. In a linear model of RSD (Kaiser 1987):

$$\tilde{\delta}_{g,1}(\boldsymbol{k}) = (b_1 + f \mu^2) \, \tilde{\delta}_m(\boldsymbol{k})$$
$$\tilde{\delta}_{g,2}(\boldsymbol{k}) = (b_2 + f \mu^2) \, \tilde{\delta}_m(\boldsymbol{k}), \tag{1}$$

where $\tilde{\delta}_m(\boldsymbol{k})$ is the corresponding (unknown) Fourier amplitude of the underlying matter overdensity field, which encodes the contribution of sample variance. The ratio of these measurements

$$\frac{\tilde{\delta}_{g,1}(\boldsymbol{k})}{\tilde{\delta}_{g,2}(\boldsymbol{k})} = \frac{1 + \frac{f}{b_1} \mu^2}{\frac{b_2}{b_1} + \frac{f}{b_1} \mu^2} \tag{2}$$

in which we divide quantities on the right-hand side of the equation by b_1 to clarify the observable combinations does not contain the unknown quantity $\tilde{\delta}_m(\boldsymbol{k})$, and is exactly known in this idealized case. By comparing measurements of this ratio at different values of μ, the quantities b_2/b_1, f/b_1 and f/b_2 may be precisely determined.

There are a number of practical obstacles to realizing the advantages outlined in the previous paragraph. First, there is an additional stochastic error component to equation (1), for example due to galaxy 'shot noise', that imposes a floor to the potential gains. Hence, multiple-tracer techniques demand high number-density galaxy surveys in order to be effective. Secondly, the expected gains scale rapidly with the difference in galaxy bias factors, through the strength of the variation of equation (2) with μ (with no gain if $b_2 = b_1$). The realization of this benefit conflicts somewhat with the high number-density requirement, given that the number density of dark matter haloes rapidly diminishes with increasing bias. Also, although magnitude-limited galaxy surveys span a wide range of galaxy luminosities (hence bias factors), there is typically a strong luminosity–redshift correlation such that at a given redshift the range of overlapping luminosities may be relatively small. Thirdly, equation (1) is only a good description of galaxy clustering in the large-scale limit. At smaller scales, non-linear processes become increasingly important, weakening the shared imprint of sample variance. Fourthly, realistic survey geometries render it impossible to measure directly the quantities of equation (1): the underlying Fourier modes are convolved with a survey selection function, such that measured power at some wavevector depends on the underlying power at a range of different wavevectors.

With all this said, the potential benefits of multiple-tracer surveys are such that they are worth exploring in detail. Indeed, although there have been a number of studies of the theoretical implications of the multiple-tracer technique, no analysis of data has yet been presented. In this study, we remedy this gap by applying a multiple-tracer power-spectrum analysis to one of the only high number-density galaxy surveys at intermediate redshifts, the Galaxy and Mass Assembly (GAMA) survey (Driver et al. 2011). We explore the resulting improvements in growth-rate measurements and search for systematic differences between results based on different galaxy populations.

Our paper is structured as follows. Section 2 provides an overview of our implementation of the multiple-tracer method, explaining how it differs from the illustrative equation (2) above. Section 3 describes the GAMA survey data, the determination of the selection function, the clustering measurements of different tracers and their covariances. In Section 4, we fit RSD models to these measurements and compare the parameter fits resulting from single-tracer and multiple-tracer analyses. In Section 5, we validate our investigations using mock catalogues derived from *N*-body simulations, and in Section 6 we test our conclusions and compare with other survey designs using Fisher matrix forecasts. Section 7 summarizes our results.

2 OVERVIEW OF ANALYSIS METHOD FOR CORRELATED TRACERS

Before proceeding, we present an overview of our practical implementation of the original insight of McDonald & Seljak (2009). First, rather than basing our analysis on the one-point statistics of the density illustrated by equation (1), it is more convenient to employ two-point clustering statistics (we use the density power spectrum). In a Fisher matrix sense, the one-point statistics of $(\tilde{\delta}_{g,1}, \tilde{\delta}_{g,2})$ and the two-point statistics described by the auto-power spectra and cross-power spectrum of the two tracers (P_1, P_2, P_c) contain identical information. Moreover, Fourier density modes may be binned when measuring the power spectra, rendering the computation of a model likelihood using the covariance matrix of the data tractable, given the complicating effects of the realistic survey selection function.

Secondly, we avoid taking a ratio of observables such as equation (2), even though this explicitly illustrates the removal of sample variance. Using a ratio in practice can lead to larger and non-Gaussian errors, and the effects of the survey selection function imply that the sample variance would not precisely cancel. We instead model the correlations between the tracer power spectra, induced by the common sample variance, in the full covariance matrix of the observables.

As a pedagogical illustration of our analysis method (see also Bernstein & Cai 2011), we consider auto-power spectrum measurements of two tracers in a Fourier bin containing M modes:

$$P_1 = (b_1 + f\mu^2)^2 P_m (1 + \alpha) + \epsilon_1$$
$$P_2 = (b_2 + f\mu^2)^2 P_m (1 + \alpha) + \epsilon_2, \qquad (3)$$

where P_m is the theoretical mean matter power spectrum in the bin, which is assumed to be known exactly, α is the (single) fluctuation from sample variance, which has a variance $\sigma^2 = 1/M$, and (ϵ_1, ϵ_2) represent independent measurement errors (e.g. from shot noise) such that $\langle\epsilon_1\rangle = \langle\epsilon_2\rangle = \langle\epsilon_1\epsilon_2\rangle = 0$. By analogy with equation (2), we consider estimating the quantities $A = (b_1 + f\mu^2)^2$ and $B = (b_2 + f\mu^2)^2$. Noting that P_1/P_m is equal to the true value of A, plus the independent fluctuations $A_{\text{true}}\alpha + \epsilon_1/P_m$ (with zero mean), the variance and covariance of the estimates of A and B are

$$\sigma_A^2 = A^2\sigma^2 + \langle\epsilon_1^2\rangle/P_m^2$$
$$\sigma_B^2 = B^2\sigma^2 + \langle\epsilon_2^2\rangle/P_m^2$$
$$\sigma_{AB}^2 = AB\sigma^2. \qquad (4)$$

In the limit of small measurement error ($\langle\epsilon_i^2\rangle \to 0$), the fractional variances in A and B are both the sample variance σ^2 – but in this limit, the correlation coefficient between A and B, $\sigma_{AB}/\sqrt{\sigma_A\sigma_B}$, tends to unity. The variance in the ratio A/B is then

$$\text{Var}(A/B) = (A/B)^2 \left[\langle\epsilon_1^2\rangle/A^2 P_m^2 + \langle\epsilon_2^2\rangle/B^2 P_m^2\right]. \qquad (5)$$

This contains no contribution from sample variance (is independent of α), reproducing the McDonald–Seljak result.

By using the power spectrum, rather than the density modes, we have thrown away phase information. But the reason that the McDonald–Seljak method allows us to evade the sample variance limit is that both tracers follow the same structure; thus, a key aspect of the method is that the phase of a given Fourier mode will be the same, independent of tracer. Since the power spectrum does not use this fact, it may seem that we have not used the method properly and may not suppress sample variance in the desired way. In fact, the phase adds no extra information to this particular analysis since

it is part of the sample variance that is cancelled in any case when forming the original ratio in equation (2).

In the equations above, we have just considered the two auto-power spectra, $P_1 = |\tilde{\delta}_1|^2$ and $P_2 = |\tilde{\delta}_2|^2$. What is the role of the cross-power spectrum $P_c = \text{Re}\{\tilde{\delta}_1\tilde{\delta}_2^*\}$? In our above model, this would be

$$P_c = (b_1 + f\mu^2)(b_2 + f\mu^2) P_m (1 + \alpha) + \epsilon_c. \qquad (6)$$

When the measurement errors are small, $P_c = \sqrt{P_1 P_2}$ and there is no extra information in the cross-power spectrum. However, determination of the cross-power spectrum does provide some independent validation of the underlying assumption of a close correlation between the two tracers (e.g., scrambling the phases of $\tilde{\delta}_1$ and $\tilde{\delta}_2$ would leave the auto-power spectrum measurements unchanged, but yield zero cross-power) and, furthermore, serves to test the assumption of linear galaxy bias. We note that for data sets where the measurement errors ϵ are not negligible, the cross-power spectrum adds information to the parameter determinations. In Section 6, we use a full Fisher matrix analysis to consider this point further.

The measurement errors for the GAMA data set analysed in this study are sufficiently small that the cross-power spectrum adds negligible information (improving the determination of the growth rate by only 0.2 per cent according to the Fisher matrix forecasts presented in Section 6 below). Indeed, its inclusion in the primary analysis causes technical difficulties with inverting the relevant covariance matrices, which are nearly singular. Therefore, although for completeness we present full derivations of the covariances including the cross-power spectrum, we restrict our parameter fits to the auto-power spectra of the two tracers and use the cross-power spectrum solely for validation of the method.

3 POWER-SPECTRUM DATA

3.1 GAMA survey

The GAMA project (Driver et al. 2011) is a multiwavelength photometric and spectroscopic survey. The redshift survey, which has been carried out with the Anglo-Australian Telescope (AAT), has provided a dense, highly complete sampling of the large-scale structure up to redshift $z \sim 0.5$. The primary target selection is $r < 19.8$ (where r is an extinction-corrected SDSS Petrosian magnitude).

In this study, we analysed a highly complete subsample of the latest survey data set, known as the GAMA II equatorial fields. This subsample covers three 12×5 deg^2 regions centred at 09^h, 12^h and 14^{h}30^m which we refer to as G09, G12 and G15, respectively. The GAMA I target selection is described by Baldry et al. (2010) and GAMA II by Liske et al. (in preparation). For GAMA II, the fields were widened by 1° and the r-band selection magnitude was changed from SDSS DR6 to DR7 (updated to ubercalibration; Abazajian et al. 2009). We restricted the input catalogue to $r < 19.8$ and only included targets that satisfied the r-band star–galaxy separation; this excluded some $J - K$ selection because the near-IR photometry had significant missing coverage. We obtained the GAMA II data from `TilingCatv41`, selecting 185 052 targets (`SURVEY_CLASS` $\geq$5).

Papers based on GAMA I data had used redshifts obtained from a semi-automatic code, `runz`, involving some user interaction. The redshifts for GAMA II (`TilingCatv41`), used here, have been updated using a fully automatic cross-correlation code that can robustly measure absorption and emission line redshifts (Baldry et al., in preparation). This significantly improved the reliability of the measured redshifts from the AAT. We restricted the redshift
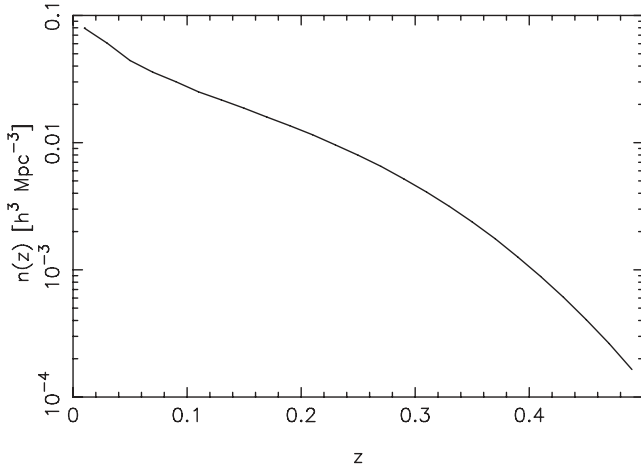
Figure 1. The average number density of GAMA galaxies as a function of redshift. This plot is constructed by combining data in the three survey regions.
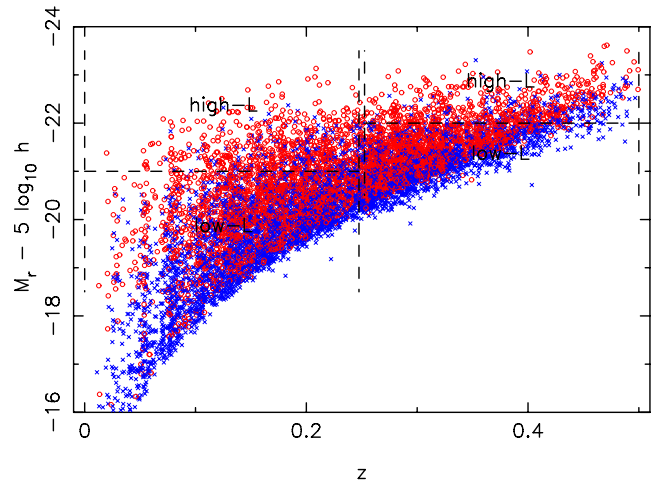

Figure 2. The distribution of absolute magnitudes M_r and redshifts z for the GAMA galaxies used in our analysis, which satisfy the selection criteria described in the text. The blue and red colour subsamples are plotted as crosses and open circles, respectively, and illustrated by appropriate colouring of the data points. The 'high-L' and 'low-L' subsamples are shown by the ranges indicated in the figure. In this plot, the galaxies have been randomly subsampled by a factor of 20, for clarity.

catalogue to galaxies with 'good' redshifts ($\mathtt{NQ} \geq 3$) in the range $0.002 < z < 0.5$. In the (G09, G12, G15) regions, we utilized (57 194, 61 278, 60 107) galaxies in our analysis. *K*-corrections were calculated with $\mathtt{kcorrect\_v4.2}$ (Blanton & Roweis 2007) using SDSS model magnitudes (see Loveday et al. 2012 for more details). Fig. 1 displays the average number density of these GAMA galaxies as a function of redshift, illustrating the high values available for our analysis, which exceed $10^{-2}\,h^3\,\mathrm{Mpc}^{-3}$ in the range $z < 0.25$.

We performed clustering measurements of galaxies in two independent redshift ranges $0 < z < 0.25$ and $0.25 < z < 0.5$. For each redshift range, we split the data into two subsamples in order to apply multiple-tracer techniques. We considered splits by colour and luminosity. First, we divided galaxies into two colour classes, 'red' and 'blue', using a redshift-dependent division in the observed colour

$$g - i = 0.8 + 3.2\,z \tag{7}$$

which traces a clear bimodality in the observed GAMA colour distribution at all redshifts. Here, *g* and *i* are model magnitudes in the appropriate bands. Alternatively, we explored splitting galaxies into two luminosity classes based on the rest-frame absolute magnitude in the *r* band. For the redshift ranges ($0 < z < 0.25$, $0.25 < z < 0.5$), we take these luminosity divisions at $M_r - 5\log_{10}h = (-21, -22)$. Fig. 2 illustrates the luminosity–redshift distribution of GAMA galaxies, colour-coded to indicate galaxies selected as 'red' and 'blue'.

3.2 Survey selection function

In order to quantify the GAMA galaxy clustering, we must first define the survey selection function which describes the expected galaxy distribution in the absence of clustering. We separated this selection function into independent angular and radial components.

The angular selection function for each GAMA region describes the exact sky coverage of the input target imaging catalogues, together with the small fluctuations in the redshift completeness of the spectroscopic follow-up. We used the masks and software available in the survey data base, $\mathtt{completeness\_maps:software:mask\_redshift\_r}$ and $\mathtt{completeness\_maps:software:mask\_sdss}$, to produce angular completeness maps in (RA, Dec.) on a fine pixel grid. These

maps are displayed in Fig. 3, in which we note the very high level of redshift completeness across each survey region, with a mean value of 97 per cent.

We determined the radial selection function of a given colour or luminosity subsample using an empirical smooth fit to the observed galaxy redshift distribution $N(z)$ of that subsample. Measurements of $N(z)$ in individual GAMA regions contain significant fluctuations; we reduced this by combining the three regions. We found that the model

$$N(z) \propto \left(\frac{z}{z_0}\right)^{\alpha} \mathrm{e}^{-(z/z_0)^{\beta}} \tag{8}$$

provided a good fit to all the relevant redshift distributions in terms of the three parameters (z_0, α, β). Fig. 4 displays an example of this model fitted to all GAMA galaxies in our sample (normalized such that $\int N(z)\,\mathrm{d}z = 1$).

Using the survey selection function, we can visualize the galaxy overdensity field within each region. For the purposes of this calculation, we binned the galaxy distribution and normalized selection function in a 3D comoving coordinate grid, denoting these gridded distributions as *D* and *R*, and then determined the overdensity field δ by smoothing these distributions with a Gaussian kernel $G(\boldsymbol{x}) = \mathrm{e}^{-(\boldsymbol{x} \cdot \boldsymbol{x})/2\lambda^2}$ such that $\delta = \mathrm{smooth}(D)/\mathrm{smooth}(R) - 1$ and $\langle \delta \rangle = 0$.

Using the $0 < z < 0.25$ redshift interval of the G09 region for illustration, Fig. 5 compares the smoothed galaxy density fields determined from the blue and red galaxy subsamples for $\lambda = 2$ and $5\,h^{-1}$ Mpc, illustrating that qualitatively these two populations are tracing the same underlying large-scale structure. Fig. 6 quantifies this observation by measuring the cross-correlation coefficient between the red and blue galaxy overdensity fields $r = \langle \delta_1 \delta_2 \rangle / \sqrt{\langle \delta_1^2 \rangle \langle \delta_2^2 \rangle}$ as a function of the smoothing scale λ. We again analysed a $0 < z < 0.25$ redshift slice, computing the cross-correlation coefficient over all three survey regions. The errors in the measurements were determined by jack-knife methods (using 100 jack-knife partitions per survey region). The cross-correlation coefficient rises to $r > 0.9$ on scales $\lambda > 5\,h^{-1}$ Mpc, dropping
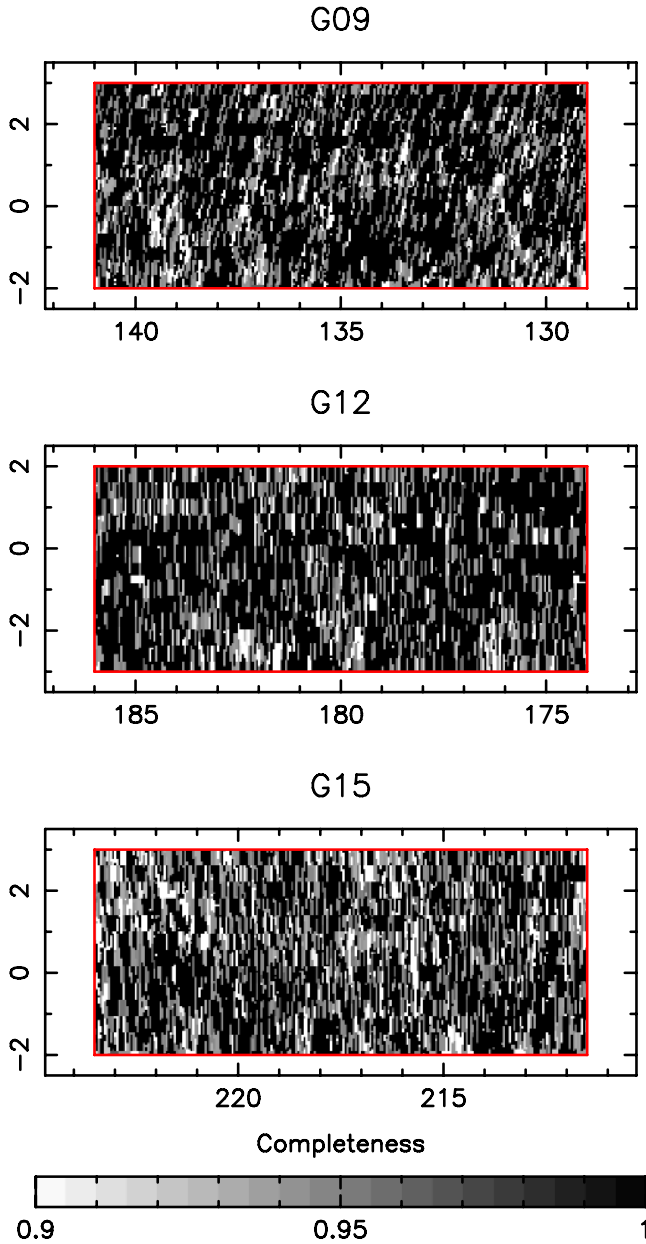
Figure 3. The angular completeness maps for each of the GAMA regions analysed in this study. The *x*- and *y*-axes correspond to RA and Dec. coordinates, respectively, in degrees.

Peacock (1994, hereafter FKP), which we generalized to cross-power spectra (also see Smith 2009).

First, we converted the galaxy distribution in a particular region to comoving coordinates, assuming a fiducial flat Λ cold dark matter (ΛCDM) cosmology with matter density $\Omega_m = 0.27$. We then enclosed the survey cone within the relevant redshift interval by a cuboid of sides (L_x, L_y, L_z) with volume $V = L_x L_y L_z$, and gridded the galaxy catalogue in cells numbering (n_x, n_y, n_z) using nearest grid point assignment to produce distributions $N_1(\boldsymbol{x})$ and $N_2(\boldsymbol{x})$ for the two tracers. The cell dimensions were chosen such that the Nyquist frequencies in each direction (e.g. $k_{\mathrm{Nyq},x} = \pi n_x / L_x$) exceeded the maximum frequency of measured power by a factor of at least 4.

We then applied a fast Fourier transform (FFT) to the gridded data, weighting each pixel by factors $w_1(\boldsymbol{x})$ and $w_2(\boldsymbol{x})$ for the two tracers, respectively:

$$\mathrm{FFT}(N_{w,\alpha}) \equiv \tilde{N}_{w,\alpha}(\boldsymbol{k}) = \sum_{\boldsymbol{x}} w_\alpha(\boldsymbol{x})\, N_\alpha(\boldsymbol{x})\, \mathrm{e}^{i\boldsymbol{k}.\boldsymbol{x}}, \tag{9}$$

where $\alpha = 1$ or 2 labels the galaxy population in all equations in this section, and the weighting factors are given by

$$w_\alpha(\boldsymbol{x}) = \frac{1}{1 + W_\alpha(\boldsymbol{x})\, N_c\, n_\alpha\, P_0}. \tag{10}$$

In equation (10), $N_c = n_x n_y n_z$ is the total number of grid cells, n_α is the mean number density of each set of tracers and $P_0 = 5000\, h^{-3}\ \mathrm{Mpc}^3$ is a characteristic value of the power spectrum at the scales of interest [$k \sim 0.1\, h\ \mathrm{Mpc}^{-1}$; we note that this can be generalized as a function of luminosity following Percival, Verde & Peacock (2004), which is beyond the scope of the current study]. $W_\alpha(\boldsymbol{x})$ is proportional to the survey selection function at each grid cell determined in Section 3.2, normalized such that $\sum_{\boldsymbol{x}} W_\alpha(\boldsymbol{x}) = 1$.

We note that the application of FKP weighting to multiple-tracer analyses requires caution: this weighting is designed to minimize the error in the measured power spectrum by balancing the effects of sample variance and shot noise, and yet (in the ideal case) the sample variance error is suppressed by the combination of the two tracers. However, for realistic surveys with a selection function and shot noise, the sample variance is only partially suppressed. We repeated our analyses for different choices of P_0: for no weighting ($P_0 = 0$), we found that the error in the measured growth rate in the various cases increased by 30–40 per cent, whereas doubling the characteristic power to $P_0 = 10\,000\, h^{-3}\ \mathrm{Mpc}^3$ produced a result almost identical to the fiducial choice of $P_0 = 5000\, h^{-3}\ \mathrm{Mpc}^3$. We may also be concerned that the slightly different weights ($w_1 \neq w_2$) applied to each subsample, owing to their different selection functions in equation (10), may undermine the correlated sample variance and weaken the eventual growth-rate determination. In order to test this concern, we repeated the power-spectrum measurements applying an identical weight to each subsample equal to $(w_1 + w_2)/2$. We found that the error in the final growth rate was unchanged compared to our default implementation. Finally, we note that more sophisticated mass-dependent weighting schemes have been proposed by some authors (Seljak, Hamaus & Desjacques 2009; Cai, Bernstein & Sheth 2011); these will be considered in future work.

We measured the complex Fourier amplitudes of the two tracers as

$$\tilde{\delta}_\alpha(\boldsymbol{k}) = \tilde{N}_{w,\alpha}(\boldsymbol{k}) - N_\alpha\, \tilde{W}_{w,\alpha}(\boldsymbol{k}), \tag{11}$$

on smaller scales due to the effects of shot noise and the manner in which different classes of galaxy populate dark matter haloes (scale-dependent and/or stochastic galaxy bias). These analyses illustrate the strong level of correlated sample variance in the multiple GAMA galaxy populations; in the next section we quantify these effects using power-spectrum measurements.

3.3 Power-spectrum measurements

We measured the power spectra of GAMA galaxies within each separate survey region, fitted models to these measurements and combined the results of the fits assuming that each region was independent. Our measurements of the auto-power and cross-power spectra of galaxies within each GAMA region were based on the optimal-weighting estimation scheme of Feldman, Kaiser &
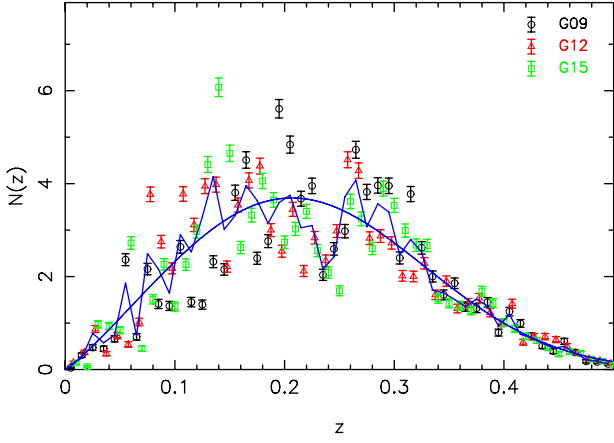
Figure 4. Determination of the radial selection function for all GAMA galaxies in our sample in the redshift interval $0 < z < 0.5$. The figure shows the redshift distributions within each of the three GAMA regions (black circles, red triangles and green squares) together with the combined $N(z)$ (jagged blue solid line) and fitted model (smooth blue solid line). The y-axis is normalized such that $\int N(z)\, dz = 1$. The plotted error bars are double the Poisson error predicted from the number of counts in each bin, noting that this is subdominant to the region-to-region fluctuations. At higher redshifts $z > 0.35$, the extra available cosmic volume results in these fluctuations becoming less significant.

where N_α is the total number of galaxies for population α and $\tilde{W}_{w,\alpha}$ is the FFT of the weighted selection function

$$\mathrm{FFT}(W_{w,\alpha}) \equiv \tilde{W}_{w,\alpha}(\boldsymbol{k}) = \sum_{\boldsymbol{x}} w_\alpha(\boldsymbol{x})\, W_\alpha(\boldsymbol{x})\, e^{i\boldsymbol{k}.\boldsymbol{x}}. \tag{12}$$

Fig. 7 compares the moduli $|\tilde{\delta}_\alpha|$ and phases ϕ_α of the complex Fourier amplitudes $\tilde{\delta}_\alpha = |\tilde{\delta}_\alpha|\, e^{i\phi_\alpha}$ for the red and blue galaxy subsamples for the $0 < z < 0.25$ redshift interval. The common sample variance induces clear correlations between the moduli and phases of the different populations.

In Appendix A, we derive the estimators of the two auto-power spectra, $P_1(\boldsymbol{k})$ and $P_2(\boldsymbol{k})$, and cross-power spectrum $P_c(\boldsymbol{k})$. The final

Figure 6. The cross-correlation coefficient in configuration space between the red and blue galaxy overdensity fields, as a function of the smoothing length λ of a Gaussian kernel. These measurements correspond to a redshift interval $0 < z < 0.25$ combining all three GAMA regions, and illustrate the high level of correlated sampled variance in the GAMA galaxy subsamples.

expressions are

$$\hat{P}_\alpha(\boldsymbol{k}) = \frac{V\left[|\tilde{\delta}_\alpha(\boldsymbol{k})|^2 - N_\alpha \sum_{\boldsymbol{x}} W_\alpha\, w_\alpha^2\right]}{N_c\, N_\alpha^2 \sum_{\boldsymbol{x}} W_\alpha^2\, w_\alpha^2}$$

$$\hat{P}_c(\boldsymbol{k}) = \frac{V\, \mathrm{Re}\left\{\tilde{\delta}_1(\boldsymbol{k})\, \tilde{\delta}_2^*(\boldsymbol{k})\right\}}{N_c\, N_1\, N_2 \sum_{\boldsymbol{x}} W_1\, w_1\, W_2\, w_2}. \tag{13}$$

We note that the expectation values of the estimators in equation (13) are a convolution of the underlying model power spectra:

$$\langle \hat{P}_\alpha(\boldsymbol{k}) \rangle = \frac{V^3}{(2\pi)^3} \int P_\alpha(\boldsymbol{k}')\, |\tilde{n}_{w,\alpha}(\delta\boldsymbol{k})|^2\, d^3\boldsymbol{k}'$$

$$\langle \hat{P}_c(\boldsymbol{k}) \rangle = \frac{V^3}{(2\pi)^3} \int P_c(\boldsymbol{k}')\, \mathrm{Re}\left\{\tilde{n}_{w,1}(\delta\boldsymbol{k})\, \tilde{n}_{w,2}^*(\delta\boldsymbol{k})\right\}\, d^3\boldsymbol{k}', \tag{14}$$
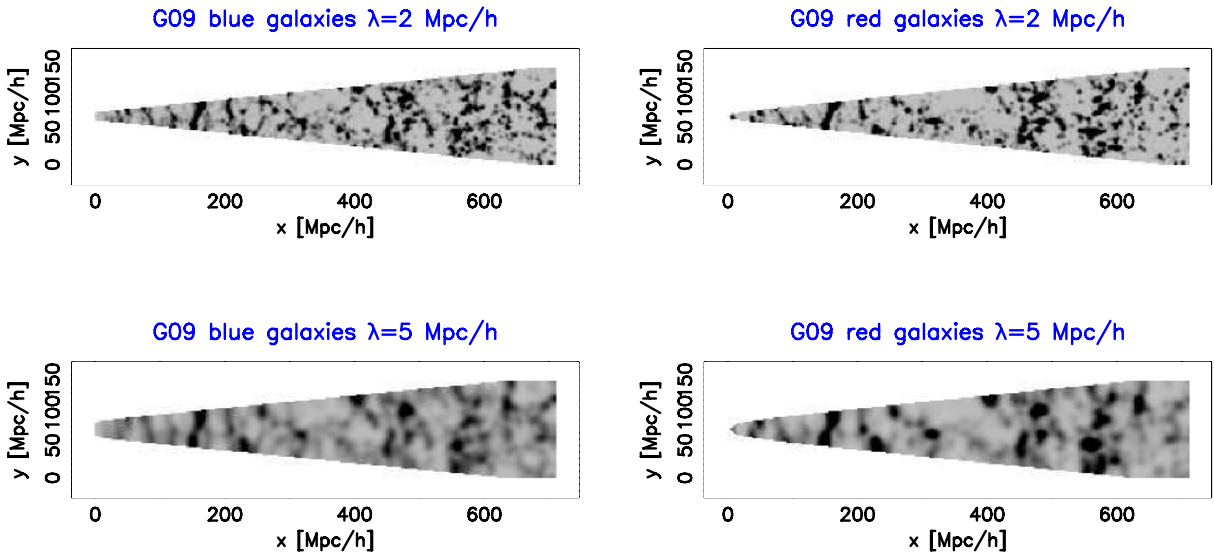

Figure 5. The galaxy overdensity field within the G09 region, determined from the gridded data and selection function, and projected on to a 2D plane parallel to the line of sight (such that the x-, y- and z-axes are oriented in the redshift, right ascension and declination directions, respectively). The left-hand and right-hand panels show the measurements for blue and red galaxies, respectively. The top and bottom rows illustrate two choices of smoothing scale, 2 and $5\, h^{-1}$ Mpc. Qualitatively, it can be seen that the different galaxy subsamples are tracing the same underlying large-scale structure.
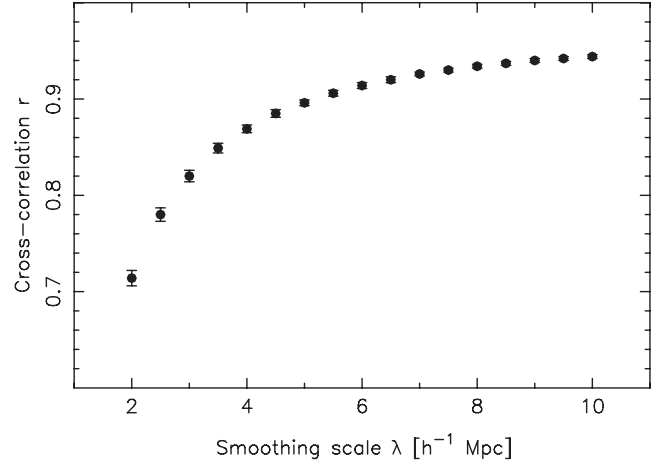
Figure 7. A mode-by-mode comparison of the moduli $|\tilde{\delta}(\boldsymbol{k})|$ and phases $\phi(\boldsymbol{k})$ of the complex Fourier amplitudes $\tilde{\delta}(\boldsymbol{k})$ estimated for the red and blue galaxy subsamples for the redshift interval $0 < z < 0.25$. The points are coded by plotting symbol and colour into four wavenumber bins in the range $k < 0.2\,h\,\mathrm{Mpc}^{-1}$. We note the strong correlations between the measurements of a given Fourier amplitude for the two different tracers. In the right-hand panel, the data points which appear in the upper-left and lower-right corners result from the 2π wrapping of the phases and support the correlation.

where $\tilde{n}_{w,\alpha} = N_\alpha\,\tilde{W}_{w,\alpha}$ and $\delta\boldsymbol{k} = \boldsymbol{k}' - \boldsymbol{k}$. We averaged the power-spectrum amplitudes for the different Fourier modes in bins of wavevector perpendicular and parallel to the line of sight, $(k_\perp, k_\parallel)$. Since in our analysis we orient the x-axis parallel to the line of sight to the centre of each survey region, and each region has a narrow and deep geometry, we can make the flat-sky approximation $k_\perp = \sqrt{k_y^2 + k_z^2}$, $k_\parallel = |k_x|$ (noting that any resulting systematic distortion is negligible compared with the sample variance error in our measurements). We used wavevector bins of width $\Delta k_\perp = \Delta k_\parallel = 0.05\,h\,\mathrm{Mpc}^{-1}$ in the analysis, only considering bins for which $|k| = \sqrt{k_\perp^2 + k_\parallel^2} < 0.3\,h\,\mathrm{Mpc}^{-1}$ because of concerns over modelling non-linearities in the power spectrum at smaller scales, which are explored further in Section 4. We also excluded the largest scale (lowest) bin in $k_\parallel$, $0 < k_\parallel < 0.05\,h\,\mathrm{Mpc}^{-1}$, whose measured power is prone to systematic effects from the radial selection function fits. The final result was a total of 22 bins. Fig. 8 displays the binned auto-power and cross-power spectrum measurements for the blue and red galaxy subsamples in the redshift interval $0.25 < z < 0.5$, for each of the three GAMA regions.

Fig. 9 displays an example of the structure of the Fourier transform of the weighted selection function, $|\tilde{W}_w(\boldsymbol{k})|^2$, which determines the relative weighting of the power-spectrum modes combined by the convolution of equation (14). As expected, this function contains a series of diminishing peaks along each axis spaced by $\Delta k = 2\pi/L$, in accordance with the dimension L of the survey cuboid parallel to that axis. These peaks are hence particularly widely spaced parallel to the narrow, declination direction of the survey geometry. This structure was fully modelled in our parameter fits. When fitting models, we recast the convolution integrals of equation (14) as matrix multiplications for reasons of numerical speed:

$$\langle \hat{P}_\alpha(i) \rangle = \sum_j (M_\alpha)_{ij}\,P_{\mathrm{mod},\alpha}(j)$$

$$\langle \hat{P}_c(i) \rangle = \sum_j (M_c)_{ij}\,P_{\mathrm{mod},c}(j), \tag{15}$$

where $(P_{\mathrm{mod},1}, P_{\mathrm{mod},2}, P_{\mathrm{mod},c})$ are the model auto-power and cross-power spectra for the two populations, evaluated at the centres of the Fourier bins. We determined the convolution matrices (M_1, M_2, M_c) by evaluating the full integrals given in equation (14) for a set of unit model vectors and tested that this produced a negligible change in results compared to implementing the full convolution.

We defined the effective redshift of each power-spectrum measurement by weighting each pixel in the 3D selection function by its contribution to the power-spectrum error:

$$z_{\mathrm{eff}}(k) = \sum_{\boldsymbol{x}} z \times \left[\frac{n(\boldsymbol{x})\,P(k)}{1 + n(\boldsymbol{x})\,P(k)} \right]^2. \tag{16}$$

We evaluated this relation at $k = 0.1\,h\,\mathrm{Mpc}^{-1}$ (although the results do not depend strongly on this choice). The effective redshifts of the measurements in the redshift intervals ($0 < z < 0.25$, $0.25 < z < 0.5$) are $z_{\mathrm{eff}} = (0.18, 0.38)$, with a very weak dependence on galaxy type.

3.4 Covariance matrix

The survey selection functions and correlated sample variance induce covariances between the estimates of the two auto-power and cross-power spectra of the galaxy populations for two Fourier modes $\boldsymbol{k}$ and $\boldsymbol{k}'$. These covariances are derived in Appendix A; the expressions for the auto-power spectrum follow Feldman et al. (1994), and to our knowledge the other formulae are new (regarding the inclusion of the selection function and weights, but also see Smith 2009). The results may be conveniently expressed in terms of the functions

$$Q_\alpha(\boldsymbol{x}) = w_\alpha^2(\boldsymbol{x})\,n_\alpha^2(\boldsymbol{x})$$

$$Q_c(\boldsymbol{x}) = w_1(\boldsymbol{x})\,n_1(\boldsymbol{x})\,w_2(\boldsymbol{x})\,n_2(\boldsymbol{x})$$

$$S_\alpha(\boldsymbol{x}) = w_\alpha^2(\boldsymbol{x})\,n_\alpha(\boldsymbol{x}). \tag{17}$$

Further defining

$$z_\alpha(\boldsymbol{k}, \boldsymbol{k}') = P_\alpha(\boldsymbol{k})\,\tilde{Q}_\alpha(\boldsymbol{k}' - \boldsymbol{k}) + \tilde{S}_\alpha(\boldsymbol{k}' - \boldsymbol{k})$$

$$z_c(\boldsymbol{k}, \boldsymbol{k}') = P_c(\boldsymbol{k})\,\tilde{Q}_c(\boldsymbol{k}' - \boldsymbol{k}) \tag{18}$$
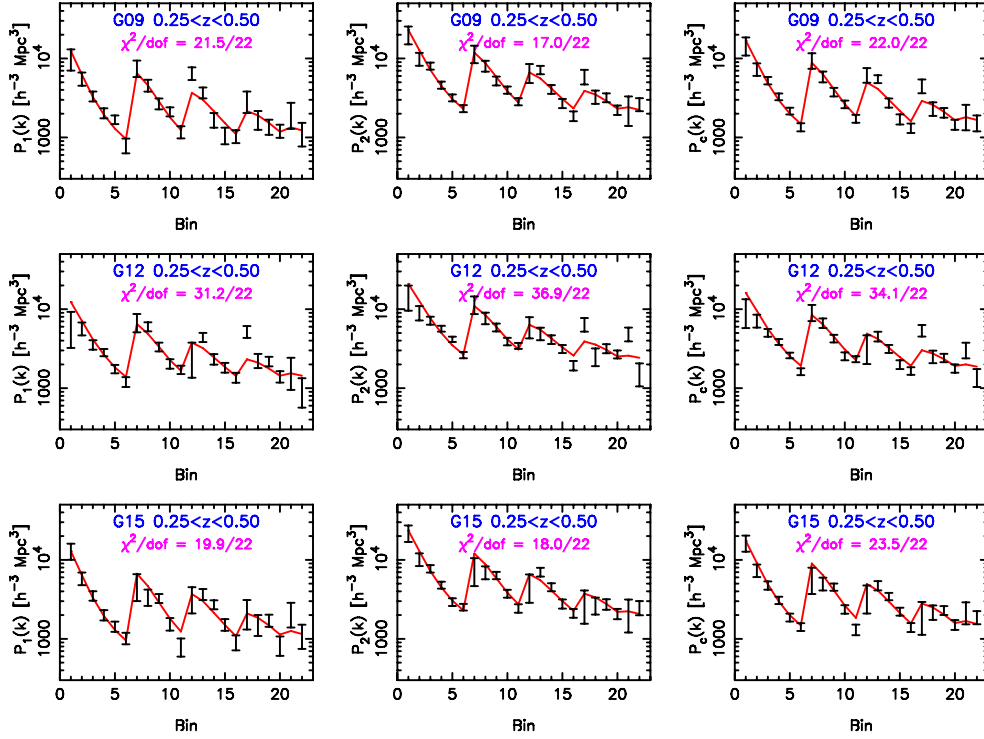
Figure 8. Measurements of the two auto-power spectra and cross-power spectrum for the blue and red subsamples of GAMA galaxies in the redshift interval $0.25 < z < 0.5$. The columns (from left to right) correspond to (P_1, P_2, P_c). The rows (from top to bottom) display the measurements for the three regions (G09, G12, G15). The solid line shows the best-fitting model (to the two auto-power spectra). The data points are ordered by looping over the bins of $k_\perp$ and then $k_\parallel$, only plotting bins for which $|k| = \sqrt{k_\perp^2 + k_\parallel^2} < 0.3\, h\,\mathrm{Mpc}^{-1}$, constituting 22 bins. The x-axis represents the bin number in the ordering, and the 'saw-tooth' pattern is produced by the repeated looping over $k_\perp$. The values of the χ^2 statistic for the model are quoted separately for each power spectrum and region.
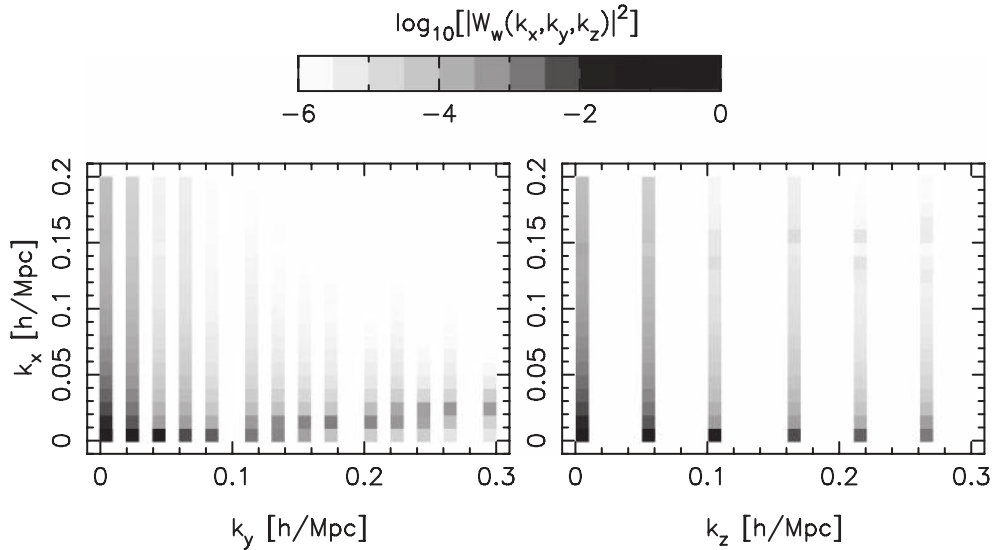

Figure 9. The structure of the Fourier transform of the weighted survey selection function, $|\tilde{W}_w(\boldsymbol{k})|^2$, which determines the relative weighting of the power-spectrum modes combined by the convolution of equation (14). As an example, we display the selection function of the 'blue' subsample for the $0.25 < z < 0.5$ redshift slice of the G09 region. We show 2D projections of this function in the space of (k_y, k_x) and (k_z, k_x), where the x-axis is oriented along the line of sight and the y- and z-axes are parallel to the (long) right ascension and (short) declination directions, respectively. The restricted y- and z-dimensions of the survey cuboid imprint a series of diminishing peaks with a regular spacing $\Delta k = 2\pi/L$. The amplitude of the function is indicated by the grey-scale shown in the upper legend; note the logarithmic scale.

the equations for the covariances in this approximation are

$$\langle \delta \hat{P}_\alpha(\boldsymbol{k}) \, \delta \hat{P}_\alpha(\boldsymbol{k}') \rangle = \frac{|z_\alpha(\boldsymbol{k}, \boldsymbol{k}')|^2}{\tilde{Q}_\alpha(0)^2}$$

$$\langle \delta \hat{P}_1(\boldsymbol{k}) \, \delta \hat{P}_2(\boldsymbol{k}') \rangle = \frac{|z_c(\boldsymbol{k}, \boldsymbol{k}')|^2}{\tilde{Q}_1(0) \, \tilde{Q}_2(0)}$$

$$\langle \delta \hat{P}_\alpha(\boldsymbol{k}) \, \delta \hat{P}_c(\boldsymbol{k}') \rangle = \frac{\mathrm{Re} \left\{ z_\alpha(\boldsymbol{k}, \boldsymbol{k}') \, z_c(\boldsymbol{k}, \boldsymbol{k}')^* \right\}}{\tilde{Q}_\alpha(0) \, \tilde{Q}_c(0)}$$

$$\langle \delta \hat{P}_c(\boldsymbol{k}) \, \delta \hat{P}_c(\boldsymbol{k}') \rangle = \frac{|z_c(\boldsymbol{k}, \boldsymbol{k}')|^2 + \mathrm{Re} \left\{ z_1(\boldsymbol{k}, \boldsymbol{k}') \, z_2(\boldsymbol{k}, \boldsymbol{k}')^* \right\}}{2 \, \tilde{Q}_c(0)^2}, \quad (19)$$

where $\delta \hat{P} = \hat{P} - \langle \hat{P} \rangle$. The derivation of these covariance relations involves the following approximations (Feldman et al. 1994).

(i) The Fourier coefficients $\tilde{\delta}(\boldsymbol{k})$ are Gaussian distributed, such that the four-point function assumes a simple form (derived in Appendix A).

(ii) The galaxy distribution forms a Poisson sample of the density field.

(iii) The power spectrum is effectively constant over the coherence scale defined by the Fourier transform of the survey selection function.

It is a useful cross-check of these equations to consider the special case of a uniform selection function and weights. In this case, $Q_\alpha = n_\alpha^2$, $Q_c = n_1 n_2$ and $S_\alpha = n_\alpha$, and the equations simplify to

$$\langle \delta \hat{P}_\alpha \, \delta \hat{P}_\alpha \rangle = \left(P_\alpha + \frac{1}{n_\alpha} \right)^2$$

$$\langle \delta \hat{P}_1 \, \delta \hat{P}_2 \rangle = P_c^2$$

$$\langle \delta \hat{P}_\alpha \, \delta \hat{P}_c \rangle = P_c \left(P_\alpha + \frac{1}{n_\alpha} \right)$$

$$\langle \delta \hat{P}_c \, \delta \hat{P}_c \rangle = \frac{1}{2} \left[P_c^2 + \left(P_1 + \frac{1}{n_1} \right) \left(P_2 + \frac{1}{n_2} \right) \right]. \quad (20)$$

In physical terms, the covariance within each auto-power spectrum is driven by a combination of sample variance (P_α) and shot noise ($1/n_\alpha$). The covariance between different auto-power spectra does not involve shot noise (since each galaxy can only appear in one subsample) but depends on sample variance via the cross-power spectrum (P_c). Covariances involving the cross-power spectrum are more complicated, involving both sample variance and shot noise contributions.

We note an important technical difficulty that arises when inverting the full covariance matrices for the two auto-power spectra and cross-power spectrum. In the approximation of linear bias and common non-linear RSD damping (see Section 4), the cross-power spectrum is a simple geometric mean of the two auto-power spectra: $P_c = \sqrt{P_1 P_2}$. In the limit of high galaxy number density, such that shot noise is negligible, the cross-power spectrum measurement then adds no information to that already present in the two auto-power spectra. We can verify this mathematically by taking the limit of equation (20) as $n_\alpha \to \infty$. The covariance matrix for the measurement of (P_1, P_2, P_c) for a single Fourier mode becomes

$$C(\boldsymbol{k}) = \begin{pmatrix} P_1^2 & P_c^2 & P_1 P_c \\ P_c^2 & P_2^2 & P_2 P_c \\ P_1 P_c & P_2 P_c & \frac{1}{2} \left(P_c^2 + P_1 P_2 \right) \end{pmatrix} \quad (21)$$

which, given that $P_c^2 = P_1 P_2$, implies that $|C| = 0$ and the matrix is singular. (The fact that the cross-power spectrum adds no information as $n_\alpha \to \infty$ is also demonstrated later by the Fisher matrix calculations in Section 6.)

The number densities of the GAMA multiple-tracer populations are well within the regime where the contribution of the cross-power spectrum to the parameter constraints is negligible, and in fact we found that the full covariance matrix was not always positive definite (even for finite n_1 and n_2). We traced the cause of this issue as the approximation made in equations (A23) and (A38) which results in the covariance matrix of equation (19); evaluating instead the exact expressions in equations (A22) and (A37) produced a positive-definite covariance matrix but was significantly more time consuming. We therefore restricted our fits to the two GAMA auto-power spectra and excluded the cross-power spectrum; the growth-rate error predicted by the Fisher matrix is worsened by only 0.2 per cent for the GAMA survey specifications. We note that, as justified by the Fisher matrix forecasts below, the cross-power spectrum does add significant information for galaxy samples with lower number densities ($n < 3 \times 10^{-4} \, h^3 \, \mathrm{Mpc}^{-3}$).

We instead used the measured cross-power spectrum to provide some independent validation of the modelling assumptions. As an example, the right-hand column of Fig. 8 compares the cross-power spectrum measurements to the model fitted to the two auto-power spectra, finding satisfactory agreement as judged by the values of the χ^2 statistic.

For model fitting, we defined a total data vector in which the measurements of the two auto-power spectra were concatenated into a longer vector $\hat{y}_i \equiv [\hat{P}_1(i), \hat{P}_2(i)]$ (for the binned measurements) and $\hat{y}(\boldsymbol{k}) \equiv [\hat{P}_1(\boldsymbol{k}), \hat{P}_2(\boldsymbol{k})]$ (for the original Fourier modes). Given that the binned estimates of power are averages within each Fourier bin $\hat{y}_i = (1/m_i) \sum_k \hat{y}(\boldsymbol{k})$, where the sum is over the m_i Fourier modes $\boldsymbol{k}$ lying in bin i, then the covariance of the binned estimates is

$$C_{ij} = \langle \delta \hat{y}_i \, \delta \hat{y}_j \rangle = \frac{1}{m_i \, m_j} \sum_{k,k'} \langle \hat{y}(\boldsymbol{k}) \, \hat{y}(\boldsymbol{k}') \rangle. \quad (22)$$

We evaluated these covariance relations over the FFT grids for each GAMA region, using equation (19). Fig. 10 illustrates the structure of the resulting covariance matrices for the $0.25 < z < 0.5$ auto-power spectrum measurements, with each displayed as a correlation matrix $C_{ij}/\sqrt{C_{ii} \, C_{jj}}$. We note the characteristic structure of diagonals, with strong correlations between different statistics measured in the same Fourier bins, and weaker correlations between different Fourier bins.

We tested our determination of the covariance matrix using a large ensemble of lognormal realizations. For each realization, two (correlated) populations of galaxies were created by Poisson sampling the same underlying density field using the GAMA survey selection functions. The diagonal and off-diagonal amplitudes of the lognormal and analytic covariance matrices were in good agreement, with the numerical values of the matrix elements differing by less than 10 per cent.

4 MODEL FITS

4.1 RSD modelling

We fit the power-spectrum measurements in each GAMA region using a standard model for the redshift-space power spectrum as a function of the cosine of the angle of the Fourier wavevector to the
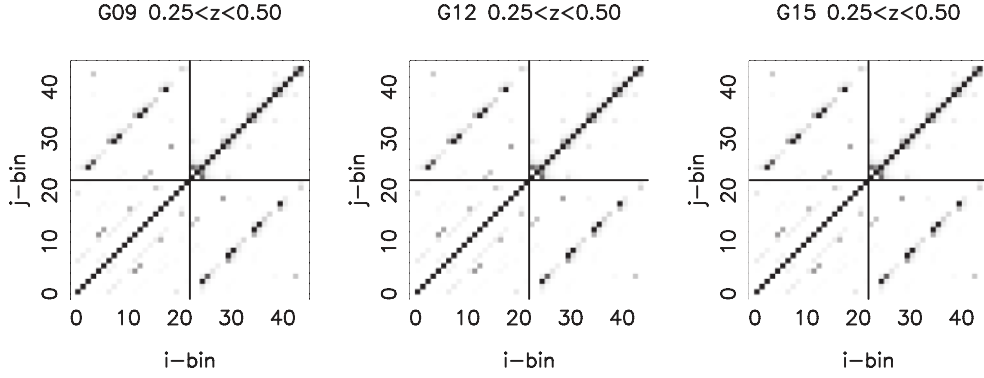
Figure 10. The correlation matrices between the two auto-power spectra of the blue and red galaxy subsamples in the redshift interval $0.25 < z < 0.5$, for the three GAMA regions. The measurements are ordered by looping over the bins of $k_\perp$ and $k_\parallel$ (only plotting bins for which $|k| = \sqrt{k_\perp^2 + k_\parallel^2} < 0.3\,h\,\mathrm{Mpc}^{-1}$, constituting 22 bins) and then concatenating these results as (P_1, P_2). The result is a 44×44 covariance matrix containing a characteristic structure of diagonals, with strong correlations between different statistics measured in the same Fourier bins and weaker correlations between different Fourier bins.

line of sight, μ:

$$P_\alpha(k, \mu) = \left[b_\alpha^2 P_{\delta\delta}(k) + 2 b_\alpha f \mu^2 P_{\delta\theta}(k) + f^2 \mu^4 P_{\theta\theta}(k) \right]$$
$$\times \, \mathrm{e}^{-k^2 \mu^2 \sigma_v^2 / H_0^2} \tag{23}$$

(Scoccimarro 2004) where, in terms of the divergence of the peculiar velocity field θ, $P_{\delta\delta}(k)$, $P_{\delta\theta}(k)$ and $P_{\theta\theta}(k)$ are the isotropic density–density, density–θ and θ–θ power spectra. This model combines the large-scale 'Kaiser limit' amplitude correction with a heuristic damping of power on smaller scales that describes a leading-order perturbation theory correction. Here, the free parameter σ_v has units of km s^{-1} and $H_0 = 100\,h$ km s^{-1} Mpc^{-1}. When fitting multiple tracers, we make the approximation that all populations of galaxies trace the same value of σ_v on large scales, as predicted by linear theory:

$$\sigma_v^2 = \frac{f^2 H_0^2}{6\pi^2} \int P_{\theta\theta}(k)\,\mathrm{d}k \tag{24}$$

although, as stated above, we treat σ_v as a free parameter to allow for non-linearities in the matter clustering. On large scales, we neglect the contribution to equation (24) from virialized galaxy motions within dark matter haloes. Approximating $P_{\theta\theta}$ as a linear power spectrum, the prediction of equation (24) in our fiducial cosmology is $\sigma_v = 334$ km s^{-1}.

We generated the matter power spectrum $P_{\delta\delta}$ in equation (23) using the 'halofit' model (Smith et al. 2003) as implemented by the CAMB software package (Lewis, Challinor & Lasenby 2000) with the cosmological parameters fixed at values inspired by fits to the cosmic microwave background fluctuations measured by *Wilkinson Microwave Anisotropy Probe* (Komatsu et al. 2011): matter density $\Omega_m = 0.27$, Hubble parameter $h = 0.719$, spectral index $n_s = 0.963$, baryon fraction $\Omega_b/\Omega_m = 0.166$ and normalization $\sigma_8 = 0.8$. We considered two different choices for producing the model velocity power spectra $P_{\delta\theta}$ and $P_{\theta\theta}$. In our fiducial model, we used the large-scale limits of the velocity power spectra $P_{\delta\theta} = P_{\theta\theta} = P_{\delta\delta}$, such that the model of equation (23) simplified to

$$P_\alpha(k, \mu) = P_{\delta\delta}(k) \left(b_\alpha + f\mu^2 \right)^2 \, \mathrm{e}^{-k^2 \mu^2 \sigma_v^2 / H_0^2}. \tag{25}$$

Secondly, we investigated whether our results changed significantly if we used the fitting formulae for $P_{\delta\theta}$ and $P_{\theta\theta}$ in terms of $P_{\delta\delta}$, calibrated by N-body simulations, proposed by Jennings, Baugh & Pascoli (2011).

Our model is hence characterized by four parameters (f, b_1, b_2, σ_v). Given that $P_{\delta\delta}(k) \propto \sigma_8^2$, where σ_8 characterizes the root-mean-square fluctuation of the matter density in spheres of radius $8\,h^{-1}$ Mpc, this parameter set may also be written as ($f\sigma_8$, $b_1\sigma_8$, $b_2\sigma_8$, σ_v). We compared the fits of the four-parameter model to the multiple tracers with fits of a three-parameter model (f, b_α, σ_v) to each individual galaxy subsample. We performed the fits by evaluating the χ^2 statistic of each model for each survey region using the full covariance matrix of equation (22):

$$\chi^2 = \sum_{ij} (\hat{y}_i - y_{\mathrm{mod},i}) \left[C^{-1} \right]_{ij} (\hat{y}_j - y_{\mathrm{mod},j}), \tag{26}$$

where in accordance with the notation of equation (22), $\hat{y}_i$ is a total data vector, concatenating the auto-power spectra of the two subsamples, and $y_{\mathrm{mod},\,i}$ is the corresponding model vector. We assumed that the measurements in each survey region were independent, and hence summed the values of χ^2 corresponding to each model.

We fit the RSD model of equation (23) to our measurements in the range $k = \sqrt{k_\perp^2 + k_\parallel^2} < 0.3\,h\,\mathrm{Mpc}^{-1}$ (noting that $\mu = k_\parallel/k$). We fixed the background cosmic expansion model and just varied the RSD parameters. It is beyond the scope of this study to consider the Alcock–Paczynski distortions that result from uncertainties in the cosmic distance scale, although we note in general that by improving measurements of the growth rate, a multiple-tracer analysis also enhances the determination of the geometrical Alcock–Paczynski distortion, leading to improved distance and expansion measurements for a galaxy sample.

We comment on the validity of the approximations of equations (23) and (25). First, in a similar analysis of the WiggleZ Dark Energy Survey, Blake et al. (2011) established that these models (including the free damping parameter) were an acceptable approximation to a large suite of other approaches for modelling non-linearities in RSD, including perturbation theory techniques. Indeed, both of these models ranked among the best performing models, as defined by the lowest values of χ^2 and the stability of the fits when increasing the maximum wavenumber fitted in the range $k_{\mathrm{max}} < 0.3\,h\,\mathrm{Mpc}^{-1}$.

Secondly, in Section 5 below we demonstrate that these techniques recovered the input growth rate (within an acceptable margin of systematic error) in mock catalogues designed with similar selection functions and galaxy bias factors as the GAMA populations. We found that the model of equation (25) produced no detectable systematic bias in the growth rate, whereas the model
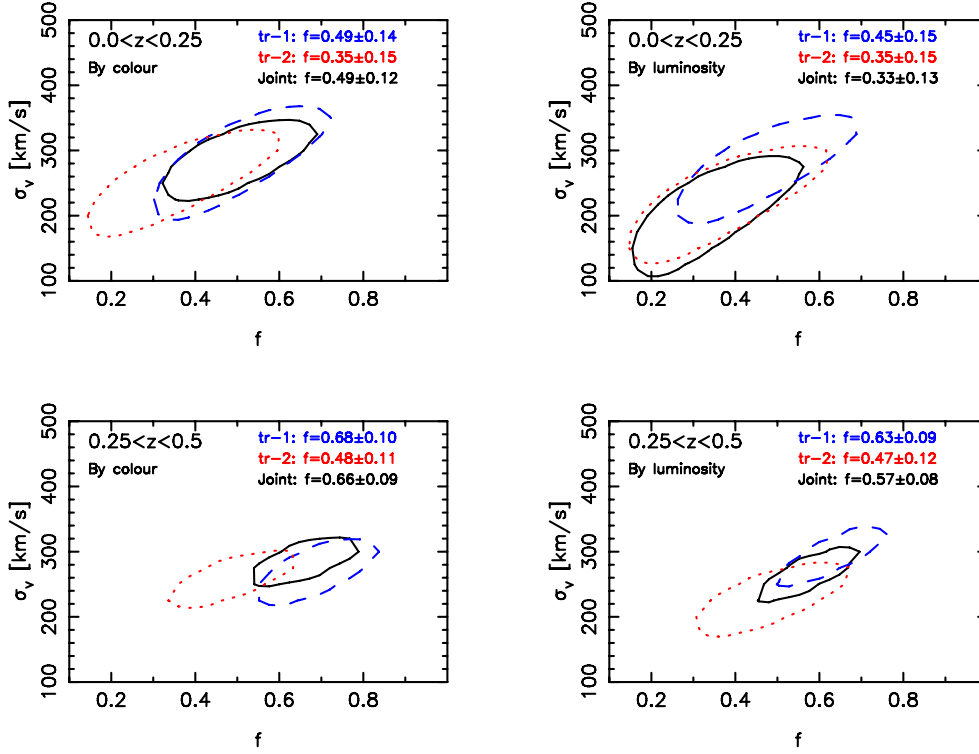
Figure 11. Fits for the RSD parameters (f, σ_v), marginalized over the galaxy bias, for different redshift ranges and multiple-tracer subsamples (split by both colour and luminosity). In each case, we compare the fits to the individual subsamples [blue dashed and red dotted contours for the low-bias ('tr-1') and high-bias ('tr-2') samples, respectively] and the joint sample (black solid contours). The likelihood contours are all 68 per cent confidence regions. The captions quote the 1D marginalized measurements of the growth rate.

of equation (23), using the Jennings et al. formulae, resulted in an overestimation of the growth rate in the simulation at a level similar to the statistical error, justifying our decision to choose equation (25) as the fiducial model. The results of these sorts of tests depend on the clustering statistic and range of scales being fitted (see also de la Torre & Guzzo 2012). At the level of statistical precision of the GAMA measurement, conclusions are unaffected by this choice of RSD model.

Thirdly, our parameter fits to the individual auto-power spectra alone produce consistent values of σ_v for each subsample, as illustrated by Fig. 11 (for the purpose of comparison with other

σ_v measurements in the literature, we note that these values are one-particle dispersions; a corresponding pairwise dispersion would be larger by a factor of $\sqrt{2}$). We explored replacing the Gaussian damping term $\mathrm{e}^{-k^2 \mu^2 \sigma_v^2/H_0^2}$ by the Lorentzian $[1 + (k\mu\sigma_v/H_0)^2]^{-1}$, finding a negligible difference in the results.

4.2 Parameter fits

In Table 1, we display the best-fitting parameters and 68 per cent confidence regions (marginalized over all other parameters) for various fits of these RSD models. For each redshift range, defining

Table 1. Fits of RSD models in single-tracer and multiple-tracer analyses of subsamples of GAMA galaxies in two different redshift intervals $0 < z < 0.25$ and $0.25 < z < 0.5$, with effective redshifts $z = 0.18$ and 0.38, respectively. Columns 3–6 display the results of fitting the four-parameter model (f, σ_v, b_1, b_2). Columns 7 and 8 show the fits of an alternative parametrization (β_1, σ_v, b_1, b_2/b_1). Column 9 provides the best-fitting values of χ^2 and corresponding numbers of degrees of freedom.

Redshift	Sample	f	σ_v (km s^{-1})	b_1	b_2	β_1	b_2/b_1	χ^2/d.o.f.
$0.0 < z < 0.25$	Blue	0.49 ± 0.14	277 ± 59	0.891 ± 0.038	–	0.56 ± 0.17	–	41.6/63
	Red	0.35 ± 0.15	246 ± 57	–	1.377 ± 0.041	–	–	53.9/63
	Joint	0.49 ± 0.12	285 ± 41	0.894 ± 0.038	1.348 ± 0.038	0.57 ± 0.15	1.509 ± 0.030	163.1/128
$0.0 < z < 0.25$	low-L	0.45 ± 0.15	267 ± 59	1.066 ± 0.039	–	0.43 ± 0.15	–	41.9/63
	high-L	0.35 ± 0.15	211 ± 62	–	1.480 ± 0.043	–	–	78.1/63
	Joint	0.33 ± 0.13	192 ± 65	1.071 ± 0.038	1.467 ± 0.039	0.32 ± 0.13	1.371 ± 0.020	175.5/128
$0.25 < z < 0.5$	Blue	0.68 ± 0.10	269 ± 34	1.074 ± 0.034	–	0.64 ± 0.10	–	90.4/63
	Red	0.48 ± 0.11	256 ± 31	–	1.707 ± 0.035	–	–	79.0/63
	Joint	0.66 ± 0.09	286 ± 23	1.105 ± 0.031	1.664 ± 0.030	0.60 ± 0.09	1.508 ± 0.027	167.7/128
$0.25 < z < 0.5$	low-L	0.63 ± 0.09	294 ± 31	1.283 ± 0.020	–	0.49 ± 0.07	–	75.6/63
	high-L	0.47 ± 0.12	224 ± 37	–	1.789 ± 0.041	–	–	75.7/63
	Joint	0.57 ± 0.08	265 ± 28	1.283 ± 0.020	1.780 ± 0.026	0.45 ± 0.07	1.388 ± 0.018	147.5/128

galaxy subsamples by either colour or luminosity, we compared fits of the three-parameter model (f, σ_v, b) to each individual auto-power spectrum with fits of the four-parameter model (f, σ_v, b_1, b_2) to the multiple-tracer auto-power spectra (with appropriate covariance). The results of these fits are shown in columns 3–6 of the table. The best-fitting values of χ^2 (and corresponding numbers of degrees of freedom) are listed in column 9; the model produces a reasonable fit to the data.

We also considered the alternative parametrization ($\beta_1, \sigma_v, b_1, b_2/b_1$) where $\beta_1 = f/b_1$, to investigate whether the multiple-tracer analysis allows the combinations of parameters f/b_1 or b_2/b_1 to be determined with any additional accuracy. These results are shown in columns 7 and 8. We found that the ratio of the galaxy bias factors of the multiple populations, b_2/b_1, was measured significantly more accurately for the multiple-tracer fits than would be obtained by a naive propagation of the errors in the individual bias factors in the single-tracer fits, but the fractional errors in measuring β_1 were similar to those in determining f. We note that the precision afforded by a multiple-tracer analysis for measuring bias ratios (which can be carried out using the 1D monopole power spectra) could provide a valuable test of models which predict the trend of bias with galaxy luminosity or colour.

Fig. 11 shows likelihood contours in the space of (f, σ_v) marginalized over the bias parameter(s), comparing the single-tracer and multiple-tracer fits. In all cases, we found that the parameter measurements from different tracers were mutually consistent, and that the fit to the combined data produced a significant shrinkage in the size of the 68 per cent confidence region. In terms of the width of the 68 per cent confidence interval for the posterior probability distribution of f, the multiple-tracer fits produced reductions in the range 10–20 per cent. In Section 6, we will demonstrate in a Fisher matrix analysis that truly large improvements in the accuracy of determination of the growth rate require higher galaxy number densities ($n > 10^{-2}\,h^3\,\mathrm{Mpc}^{-3}$).

Fig. 12 displays the marginalized measurements of the normalized growth rate $f\sigma_8(z)$ for the GAMA multiple-tracer analysis split
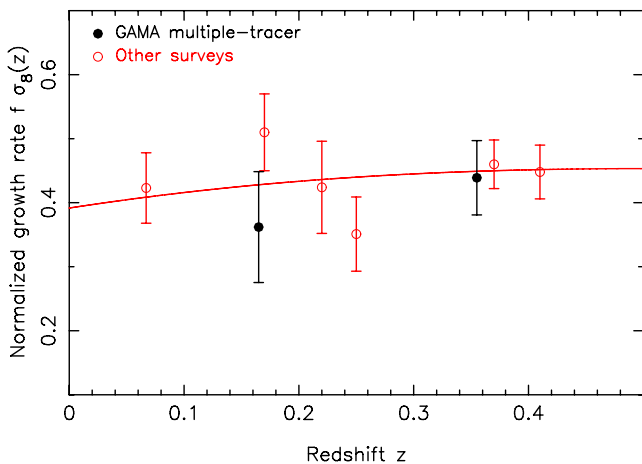

Figure 12. Marginalized measurements of the normalized growth-rate $f\sigma_8(z)$ fit to multiple-tracer GAMA galaxy subsamples split by colour. The prediction of a flat ΛCDM model with matter density $\Omega_m = 0.27$ and normalization $\sigma_8 = 0.8$ is also shown as the solid line. The open squares display the results of RSD analyses of a series of other galaxy surveys in a similar redshift range, taken from 6dFGS ($z = 0.067$; Beutler et al. 2012), 2dFGRS ($z = 0.17$; Hawkins et al. 2003), the SDSS Luminous Red Galaxy sample ($z = 0.25$ and 0.37; Samushia et al. 2012) and the WiggleZ Survey ($z = 0.22$ and 0.41; Blake et al. 2011).

by colour, compared to the prediction of a flat ΛCDM model with matter density $\Omega_m = 0.27$ and normalization $\sigma_8 = 0.8$. The measurements of $f\sigma_8(z)$ in redshift slices ($0 < z < 0.25$, $0.25 < z < 0.5$) are (0.36 ± 0.09, 0.44 ± 0.06), respectively. We compared the GAMA measurements with the published RSD analyses of a series of other galaxy surveys in a similar redshift range, which are plotted as the open squares in Fig. 12. These measurements were taken from 6dFGS ($z = 0.067$; Beutler et al. 2012), 2dFGRS ($z = 0.17$; Hawkins et al. 2003), the SDSS Luminous Red Galaxy sample ($z = 0.25$ and 0.37; Samushia et al. 2012) and the WiggleZ Survey ($z = 0.22$ and 0.41; Blake et al. 2011). Our GAMA measurements are consistent with the results of these other surveys at similar redshifts.

5 VALIDATION USING *N*-BODY SIMULATIONS

We tested the validity of the non-linear RSD model of equation (23), in particular the amplitude of any systematic modelling error that may impact the growth-rate measurements, by fitting it to power-spectrum measurements of dark matter halo catalogues generated from *N*-body simulations. We carried out these tests using the GiggleZ *N*-body simulation (Poole et al., in preparation), a 2160^3 particle dark matter simulation run in a $1\,h^{-1}$ Gpc box (with resulting particle mass $7.5 \times 10^9\,h^{-1}\,\mathrm{M}_\odot$). Bound structures were identified using SUBFIND (Springel et al. 2001), which uses a friends-of-friends (FoF) scheme followed by a substructure analysis to identify bound overdensities within each FoF halo. We employed each halo's maximum circular velocity V_{max} as a proxy for mass and used the centre-of-mass velocities for each halo when introducing RSD.

We divided the GiggleZ simulation into eight non-overlapping realizations of the GAMA survey for the redshift range $0.25 < z < 0.5$, where each realization consists of the three survey regions. (We note that since we are just using one simulation, there will be low-level correlations between these realizations deriving from common large-scale modes; hence, the scatter in results between the realizations may be slightly underestimated.) In each region, we selected two populations of haloes which approximately reproduce the bias factors of the blue and red GAMA populations, a 'low-bias' set with $80 < V_{max} < 135$ km s^{-1} and a 'high-bias' set with $135 < V_{max} < 999$ km s^{-1}, and subsampled these haloes using the full survey selection functions. We note that our intention here was not to produce full mock GAMA catalogues, since we incorporated no information about colour, luminosity or halo occupation distribution, but rather to validate that the RSD model of equation (23) was able to reproduce the input growth rate of the *N*-body simulation on quasi-linear scales, with minimal systematic error.

We measured the auto-power spectra of the two populations in each survey region for each realization and fitted the RSD model of equation (25), using the same techniques we applied when analysing the real data (using the range $k < 0.3\,h\,\mathrm{Mpc}^{-1}$). Fig. 13 shows the marginalized measurements of (f, σ_v) for each of the eight realizations, with the 68 per cent confidence region displayed as the dotted (coloured) lines. The solid black contours denote the 68 and 95 per cent confidence regions obtained by combining these eight measurements, assuming that they were independent. The vertical dashed line indicates the predicted growth rate $f = 0.69$ based on the input cosmological parameters of the *N*-body simulation (at $z = 0.408$); the fits reveal no evidence for systematic modelling errors. The average best-fitting χ^2 for the eight realizations is 91.4 for 128 degrees of freedom.

With the caveat that we only used eight realizations, we compared the errors in the measured growth rates of the simulations and
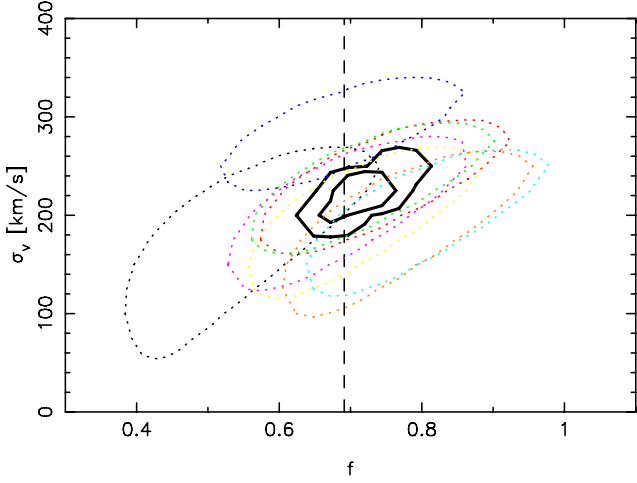
Figure 13. Growth-rate fits to multiple-tracer power spectra measured in eight different realizations of the GAMA survey extracted from a large *N*-body simulation. In each realization, two halo catalogues were extracted with bias factors close to two GAMA populations and were subsampled in three survey regions using the appropriate selection functions for the $0.25 < z < 0.5$ redshift range. The eight sets of dotted coloured contours represent the 68 per cent confidence region of (f, σ_v) fits (marginalized over bias parameters) to each of the eight realizations, using the same RSD model and fitting range as applied to the GAMA data. The solid black contours denote 68 and 95 per cent confidence regions obtained by combining these eight measurements, assuming that they were independent. The vertical dotted line shows the growth rate deduced from the input cosmological parameters of the simulation.

data. The average error in the growth rate in the fits to the mock catalogues was $\Delta f = 0.11$, compared to $\Delta f = 0.09$ for the data, and the standard deviation in the best-fitting values for each realization was $\sigma_f = 0.07$. Given that these mock catalogues do not match the galaxy populations of the data sample exactly, we consider the more conservative value obtained from the data covariance matrix to be the more reliable estimate.

6 FISHER MATRIX FORECASTS

We compared our measurements with Fisher matrix forecasts, which also indicate how our results would extend to surveys with a different design (also see McDonald & Seljak 2009; White et al. 2009; Abramo 2012). In this section, we adopt the notation P_{ij} to describe the auto-power spectra between tracers (with $j = i$) and cross-power spectra (with $j \neq i$). We assume that the covariance matrix for the measurement of (P_{11}, P_{22}, P_{12}) using an individual Fourier mode $\mathbf{k} = (k, \mu)$ can be written following equation (20) as

$$C(\mathbf{k}) = \begin{pmatrix} Q_1^2 & P_1 P_2 & Q_1\sqrt{P_1 P_2} \\ P_1 P_2 & Q_2^2 & Q_2\sqrt{P_1 P_2} \\ Q_1\sqrt{P_1 P_2} & Q_2\sqrt{P_1 P_2} & \frac{1}{2}(P_1 P_2 + Q_1 Q_2) \end{pmatrix}, \quad (27)$$

where we have written $P_i = P_{ii}$ and $Q_i = P_i + 1/n_i$, where n_i is the number density of the tracers. The RSD power-spectrum model [using equation (25) for simplicity] is then

$$P_{ij}(k, \mu) = (b_i + f\mu^2)(b_j + f\mu^2)\, P_m(k)\, e^{-k^2\mu^2\sigma_v^2/H_0^2}, \quad (28)$$

where b_i are the bias factors of the tracers. The derivatives with respect to the parameters are

$$\frac{\partial P_{ij}}{\partial f} = \left[(b_i + b_j)\mu^2 + 2f\mu^4 \right] P_m(k)\, e^{-k^2\mu^2\sigma_v^2/H_0^2}$$

$$\frac{\partial P_{ii}}{\partial b_i} = \frac{2P_{ii}}{b_i + f\mu^2}$$

$$\frac{\partial P_{ii}}{\partial b_j} = 0 \quad (j \neq i)$$

$$\frac{\partial P_{ij}}{\partial b_i} = \frac{P_{ij}}{b_i + f\mu^2} \quad (j \neq i)$$

$$\frac{\partial P_{ij}}{\partial \sigma_v^2} = -\frac{k^2\mu^2}{H_0^2} P_{ij}. \quad (29)$$

The Fisher matrix of the parameter vector $p_\alpha = (f, \sigma_v^2, b_1, b_2)$ is written as

$$F_{\alpha\beta} = \sum_{k,\mu} m(k,\mu) \sum_{i,j} \frac{\partial P_{ij}(k,\mu)}{\partial p_\alpha} \left[C(k,\mu)^{-1} \right]_{ij} \frac{\partial P_{ij}(k,\mu)}{\partial p_\beta}, \quad (30)$$

where $m(k, \mu)$ is the number of modes in a (k, μ) bin of width $(\Delta k, \Delta \mu)$, which we deduce from the survey volume V as

$$m(k, \mu) = \frac{V}{(2\pi)^3} 2\pi k^2 \Delta k\, \Delta \mu. \quad (31)$$

We considered five bins in μ in the range $0 < \mu < 1$ and six bins in k in the range $0 < k < 0.3\, h\, \mathrm{Mpc}^{-1}$, although our results were not sensitive to the bin widths. The covariance matrix of the parameters follows as $C_{\alpha\beta} = (F^{-1})_{\alpha\beta}$, and we focused in particular on the forecast error in the growth-rate measurement, $\Delta f = \sqrt{C_{11}} = (F^{-1})_{11}$.

In our fiducial model of the GAMA II survey, we fixed the RSD parameters $(f, \sigma_v) = (0.59, 300)$, number densities $n_i = 5 \times 10^{-3}\, h^3\, \mathrm{Mpc}^{-3}$, bias factors $(b_1, b_2) = (1.0, 1.4)$ and volume $V = 6.42 \times 10^6\, h^{-3}\, \mathrm{Mpc}^3$. These values are representative of the two-sample data set for $0 < z < 0.25$. The forecast marginalized error in the growth rate for this case is $\Delta f = 0.096$ for the multiple-tracer fits, and $\Delta f = 0.124$ and 0.156 for the low-bias and high-bias single-tracer fits, respectively (such that the multiple-tracer analysis produces an ≈ 20 per cent improvement compared to the low-bias case). These forecasts are a little better than, although comparable to, the measurements quoted in Table 1, and we note that the Fisher matrix forecast assumes a perfect-cuboid survey with no correlations between different Fourier modes.

We then considered two sets of variations which allow us to explore other survey designs.

(i) Varying the bias factor of the second tracer in the range $1 < b_2 < 4$ for different choices of n_2, fixing $b_1 = 1$ and $n_1 = 5 \times 10^{-3}\, h^3\, \mathrm{Mpc}^{-3}$.

(ii) Varying the number density of both tracers in the range $1 \times 10^{-4} < n_i < 5 \times 10^{-2}\, h^3\, \mathrm{Mpc}^{-3}$ for different choices of b_2, fixing $b_1 = 1$.

The results are displayed in Fig. 14, with the solid circles indicating the fiducial GAMA case quoted above.

The upper panel of Fig. 14 indicates the improvement in the multiple-tracer growth-rate measurement that results as the difference between the bias factors of the galaxy populations increases. For $n_2 = n_1 = 5 \times 10^{-3}\, h^3\, \mathrm{Mpc}^{-3}$ and $b_1 = 1$, the growth-rate measurement improves by $(8, 22, 35, 44, 51)$ per cent for $b_2 = (1.2, 1.4, 1.6, 1.8, 2.0)$. These forecast gains will be impacted by the practical difficulty of maintaining a high target number density as the galaxy bias increases, as described by the set of lines for different values of n_2 in the upper panel of Fig. 14.

The lower panel of Fig. 14 displays the increasing efficacy of the multiple-tracer method as the number density of the galaxy
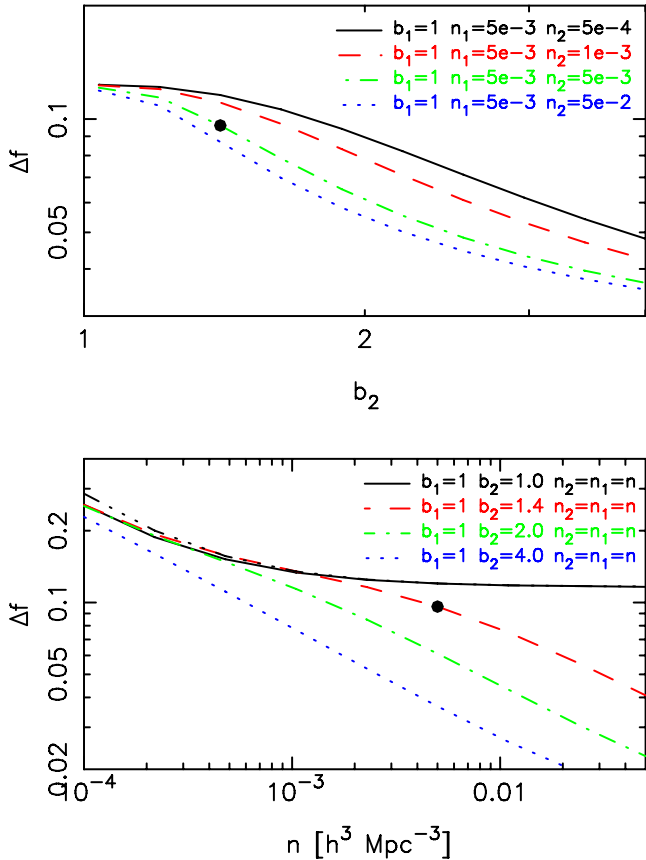
Figure 14. Fisher matrix forecasts for the error in the growth rate, Δf, marginalized over the other RSD parameters. We consider two-tracer survey configurations varying the bias parameters (b_1, b_2) and number densities (n_1, n_2), fixing the survey volume $V = 6.42 \times 10^6\, h^{-3}\,\mathrm{Mpc}^3$ and $b_1 = 1$ for all cases. In the upper panel, we fix $n_1 = 5 \times 10^{-3}\, h^3\,\mathrm{Mpc}^{-3}$ and plot Δf as a function of b_2 for various choices of n_2. In the lower panel, we plot Δf as a function of $n = n_1 = n_2$ for various choices of b_2. The triple-dot–dashed black curve in the lower panel, compared to the solid black curve, shows the effect of dropping the cross-power spectrum information. The solid circles in the panels indicate the fiducial GAMA values of these parameters. Changing the survey volume V will simply scale the results by $\Delta f \propto V^{-1/2}$.

populations increases. For $n > 10^{-3}\, h^3\,\mathrm{Mpc}^{-3}$, the gains from single-tracer RSD saturate (as indicated by the solid black line), but the growth-rate measurement from multiple tracers improves by (12, 22, 37, 53, 66) per cent for $n = (0.23, 0.5, 1.1, 2.4, 5.2) \times 10^{-2}\, h^3\,\mathrm{Mpc}^{-3}$ assuming $(b_1, b_2) = (1.0, 1.4)$. The black triple-dot–dashed line in Fig. 14, which should be compared to the black solid line, illustrates the effect of dropping the information from the cross-power spectrum. For low values of number density $n < 10^{-3}\, h^3\,\mathrm{Mpc}^{-3}$, the cross-power spectrum adds some information due to shot noise. For high number density $n > 10^{-3}\, h^3\,\mathrm{Mpc}^{-3}$, the cross-power spectrum may be entirely predicted from the two auto-power spectra (under the assumption of linear galaxy bias) and hence its inclusion does not improve the growth-rate measurements within the assumed RSD model.

7 SUMMARY

In this study, we have presented the first observational multiple-tracer analysis of RSD using data from the GAMA survey. We performed a Fourier analysis of the two auto-power spectra of galaxy

populations split by both colour and luminosity, deriving new expressions for the covariances between these measurements in terms of a general survey selection function and weighting scheme, and verified our results by also measuring the cross-power spectrum. We fit models to the redshift-space power spectra in terms of the gravitational growth rate, f, linear galaxy bias factors and an empirical non-linear damping parameter. We find that, in the case of GAMA, the multiple-tracer analysis produces an improvement in the measurement accuracy of f by 10–20 per cent (depending on the sample). The growth rates determined from the separate populations, split by colour and luminosity, are consistent, showing no evidence for strong systematic modelling errors. The precision of our measurements is similar to a Fisher matrix forecast, which indicates how our analyses would extend to surveys with a different design: for samples with higher number densities or bias factor differentials, much stronger improvements in the accuracy of growth-rate determination are expected. We tested our methodology using mock catalogues from N-body simulations, demonstrating that the systematic error in the measured growth rate was much smaller than the statistical error. The normalized gravitational growth rate determined in two independent redshift slices, $f\sigma_8(z = 0.18) = 0.36 \pm 0.09$ and $f\sigma_8(z = 0.38) = 0.44 \pm 0.06$ using multiple-tracer subsamples selected by colour, is consistent with results from other RSD surveys in a similar redshift range, and with standard ΛCDM models.

REFERENCES

Abazajian K. et al., 2009, ApJS, 182, 543
Abramo L. R., 2012, MNRAS, 420, 2042
Abramo L. R., Leonard K., 2013, MNRAS, 432, 318
Baldry I. et al., 2010, MNRAS, 404, 86
Bernstein G., Cai Y.-C., 2011, MNRAS, 416, 3009
Beutler F. et al., 2012, MNRAS, 423, 3430
Blake C. et al., 2011, MNRAS, 415, 2876
Blanton M., Roweis S., 2007, AJ, 133, 734
Cai Y.-C., Bernstein G., Sheth R., 2011, MNRAS, 412, 995
Colless M. et al., 2001, MNRAS, 328, 1039
Contreras C. et al., 2013, MNRAS, 430, 924
Cresswell J., Percival W., 2009, MNRAS, 392, 682
Dawson K. et al., 2013, AJ, 145, 10
de la Torre S., Guzzo L., 2012, MNRAS, 427, 327
de la Torre S. et al., 2013, A&A, 557, 54
Dekel A., Lahav O., 1999, ApJ, 520, 24
Drinkwater M. et al., 2010, MNRAS, 401, 1429
Driver S. et al., 2011, MNRAS, 413, 971
Feldman H., Kaiser N., Peacock J., 1994, ApJ, 426, 23

Gil-Marin H., Wagner C., Verde L., Jimenez R., Heavens A., 2010, MNRAS, 407, 772

Hamaus N., Seljak U., Desjacques V., 2012, Phys. Rev. D, 86, 3513

Hawkins E. et al., 2003, MNRAS, 346, 78

Jennings E., Baugh C. M., Pascoli S., 2011, MNRAS, 410, 2081

Jones D. H. et al., 2009, MNRAS, 399, 683

Kaiser N., 1987, MNRAS, 227, 1

Komatsu E. et al., 2011, ApJS, 192, 18

Lewis A., Challinor A., Lasenby A., 2000, ApJ, 538, 473

Loveday J. et al., 2012, MNRAS, 420, 1239

Marin F., 2011, ApJ, 737, 97

Marin F. et al., 2013, MNRAS, 432, 2654

McDonald P., Seljak U., 2009, J. Cosmol. Astropart. Phys., 10, 7

Percival W. J., Verde L., Peacock J., 2004, MNRAS, 347, 645

Reid B. et al., 2012, MNRAS, 426, 2719

Samushia L., Percival W. J., Raccanelli A., 2012, MNRAS, 420, 2102

Scoccimarro R., 2004, Phys. Rev. D, 70, 83007

Seljak U., 2009, Phys. Rev. Lett., 102, 1302

Seljak U., Hamaus N., Desjacques V., 2009, Phys. Rev. Lett., 103, 1303

Smith R. E., 2009, MNRAS, 400, 851

Smith R. E. et al., 2003, MNRAS, 341, 1311

Springel V., White S., Tormen G., Kauffmann G., 2001, MNRAS, 328, 726

Swanson M., Tegmark M., Blanton M., Zehavi I., 2008, MNRAS, 385, 1635

White M., Song Y.-S., Percival W., 2009, MNRAS, 397, 1348

Wild V. et al., 2005, MNRAS, 356, 247

York D. et al., 2000, AJ, 120, 1579

APPENDIX A: DERIVATION OF AUTO-POWER AND CROSS-POWER SPECTRUM ESTIMATORS AND COVARIANCES

A1 Fourier conventions

First we note our conventions for Fourier transforms and inverse Fourier transforms:

$$\text{FT}(y) = \tilde{y}(\boldsymbol{k}) = \frac{1}{V} \int y(\boldsymbol{x}) \, e^{i\boldsymbol{k}.\boldsymbol{x}} \, d^3\boldsymbol{x} \tag{A1}$$

$$\text{IFT}(\tilde{y}) = y(\boldsymbol{x}) = \frac{V}{(2\pi)^3} \int \tilde{y}(\boldsymbol{k}) \, e^{-i\boldsymbol{k}.\boldsymbol{x}} \, d^3\boldsymbol{k}, \tag{A2}$$

where V is the Fourier volume. Some useful relations involving the Dirac delta function δ_D and its transform are

$$\int e^{i\boldsymbol{k}.\boldsymbol{x}} \, d^3\boldsymbol{x} = V \, \tilde{\delta}_D(\boldsymbol{k}) \tag{A3}$$

$$\int e^{i\boldsymbol{k}.\boldsymbol{x}} \, d^3\boldsymbol{k} = \frac{(2\pi)^3}{V} \, \delta_D(\boldsymbol{x}) \tag{A4}$$

$$\int \delta_D(\boldsymbol{x} - \boldsymbol{x}_0) \, d^3\boldsymbol{x} = V \tag{A5}$$

$$\int y(\boldsymbol{x}) \, \delta_D(\boldsymbol{x} - \boldsymbol{x}_0) \, d^3\boldsymbol{x} = V \, y(\boldsymbol{x}_0) \tag{A6}$$

$$\int \tilde{\delta}_D(\boldsymbol{k} - \boldsymbol{k}_0) \, d^3\boldsymbol{k} = \frac{(2\pi)^3}{V} \tag{A7}$$

$$\int \tilde{y}(\boldsymbol{k}) \, \tilde{\delta}_D(\boldsymbol{k} - \boldsymbol{k}_0) \, d^3\boldsymbol{k} = \frac{(2\pi)^3}{V} \, \tilde{y}(\boldsymbol{k}_0). \tag{A8}$$

It is also useful to list our conventions for evaluating FFTs, which we will employ in practice for implementing these calculations:

$$\text{FFT}(y) = \sum_{\boldsymbol{x}_i} y(\boldsymbol{x}_i) \, e^{i\boldsymbol{k}.\boldsymbol{x}_i} \tag{A9}$$

$$\text{IFFT}(\tilde{y}) = \sum_{\boldsymbol{k}_i} \tilde{y}(\boldsymbol{k}_i) \, e^{-i\boldsymbol{k}_i.\boldsymbol{x}}. \tag{A10}$$

Noting the equivalences $(1/V) \int d^3\boldsymbol{x} \equiv (1/N_c) \sum_{\boldsymbol{x}}$ and $[V/(2\pi)^3] \int d^3\boldsymbol{k} \equiv \sum_{\boldsymbol{k}}$, we deduce that $\text{FFT}(y) = N_c \, \text{FT}(y)$ and $\text{IFFT}(\tilde{y}) = \text{IFT}(\tilde{y})$, where N_c is the total number of FFT cells.

A2 Estimator for the auto-power spectrum

We first develop the estimator for the auto-power spectrum of a galaxy number-density distribution $n(\boldsymbol{x})$, given an underlying selection function $\langle n(\boldsymbol{x}) \rangle$ describing the average over many realizations, and allowing for a general weighting function $w(\boldsymbol{x})$. This derivation follows Feldman, Kaiser & Peacock (1994) and Smith (2009); we will then provide the extension to the galaxy cross-power spectrum and the various covariances. The normalization of the number density in terms of the total number of galaxies N is such that

$$\int n(\boldsymbol{x}) \, d^3\boldsymbol{x} = N. \tag{A11}$$

First, we define the weighted galaxy overdensity

$$\delta(\boldsymbol{x}) = w(\boldsymbol{x}) \, [n(\boldsymbol{x}) - \langle n(\boldsymbol{x}) \rangle] \tag{A12}$$

and consider the Fourier transform of this expression, $\tilde{\delta}(\boldsymbol{k})$. In order to perform this evaluation, it is convenient to split the sample volume into many small cells i at positions $\boldsymbol{x}_i$ with infinitesimal volumes δV_i, such that the number of galaxies N_i in the ith cell is 0 or 1, and we can write the number-density distribution as

$$n(\boldsymbol{x}) = \frac{1}{V} \sum_i N_i \, \delta_D(\boldsymbol{x} - \boldsymbol{x}_i) \tag{A13}$$

which satisfies $\int n(\boldsymbol{x}) \, d^3\boldsymbol{x} = \sum_i N_i = N$. Writing the weighted number density $n_w(\boldsymbol{x}) \equiv w(\boldsymbol{x}) \, n(\boldsymbol{x})$, we find that

$$\tilde{n}_w(\boldsymbol{k}) = \frac{1}{V} \int n_w(\boldsymbol{x}) \, e^{i\boldsymbol{k}.\boldsymbol{x}} \, d^3\boldsymbol{x} = \frac{1}{V} \sum_i w_i \, N_i \, e^{i\boldsymbol{k}.\boldsymbol{x}_i} \tag{A14}$$

hence

$$\tilde{\delta}(\boldsymbol{k}) = \tilde{n}_w(\boldsymbol{k}) - \langle \tilde{n}_w(\boldsymbol{k}) \rangle = \frac{1}{V} \sum_i w_i \, (N_i - \langle N_i \rangle) \, e^{i\boldsymbol{k}.\boldsymbol{x}_i}. \tag{A15}$$

Then, using the fact that

$$\langle (N_i - \langle N_i \rangle)(N_j - \langle N_j \rangle) \rangle = \langle N_i \, N_j \rangle - \langle N_i \rangle \langle N_j \rangle \tag{A16}$$

we find that

$$\langle \tilde{\delta}(\boldsymbol{k}) \, \tilde{\delta}^*(\boldsymbol{k}') \rangle =$$
$$\frac{1}{V^2} \sum_{i,j} w_i \, w_j \, \left(\langle N_i \, N_j \rangle - \langle N_i \rangle \langle N_j \rangle \right) e^{i(\boldsymbol{k}.\boldsymbol{x}_i - \boldsymbol{k}'.\boldsymbol{x}_j)}. \tag{A17}$$

We evaluate this double sum by splitting it into two parts, with $j = i$ and $j \neq i$. The part of the sum with $j = i$ can be simplified using

$$\langle N_i^2 \rangle - \langle N_i \rangle^2 = \langle N_i \rangle = \langle n_i \rangle \, \delta V_i \tag{A18}$$

which holds given that $N_i^2 = N_i$ (for $N_i = 0$ or 1) and $\langle N_i \rangle^2 \propto (\delta V_i)^2$ is negligible. We can express the part of the sum with $j \neq i$ in terms of the galaxy correlation function ξ using

$$\langle N_i \, N_j \rangle - \langle N_i \rangle \langle N_j \rangle = (\langle n_i \rangle \delta V_i) \, (\langle n_j \rangle \delta V_j) \, \xi(\boldsymbol{x}_i, \boldsymbol{x}_j). \tag{A19}$$

Making these substitutions,

$$\langle \tilde{\delta}(\boldsymbol{k})\, \tilde{\delta}^*(\boldsymbol{k}')\rangle$$

$$= \frac{1}{V^2} \sum_{i \neq j} w_i\, w_j\, \langle n_i\rangle\, \langle n_j\rangle\, \delta V_i\, \delta V_j\, \xi(\boldsymbol{x}_i, \boldsymbol{x}_j)\, \mathrm{e}^{\mathrm{i}(k.x_i - k'.x_j)}$$

$$+ \frac{1}{V^2} \sum_i w_i^2\, \langle n_i\rangle\, \delta V_i\, \mathrm{e}^{\mathrm{i}(k-k').x_i}. \tag{A20}$$

Now we transform the sums into integrals and substitute the relation

$$\xi(\boldsymbol{x}, \boldsymbol{x}') = \frac{1}{(2\pi)^3} \int P(\boldsymbol{k}'')\, \mathrm{e}^{-\mathrm{i}k''.(x-x')}\, \mathrm{d}^3 \boldsymbol{k}'' \tag{A21}$$

between the correlation function and auto-power spectrum $P(k)$ in volume units. After some algebra we find

$$\langle \tilde{\delta}(\boldsymbol{k})\, \tilde{\delta}^*(\boldsymbol{k}')\rangle$$

$$= \frac{1}{(2\pi)^3} \int P(\boldsymbol{k}'')\, \tilde{n}_w(\boldsymbol{k} - \boldsymbol{k}'')\, \tilde{n}_w^*(\boldsymbol{k}' - \boldsymbol{k}'')\, \mathrm{d}^3 \boldsymbol{k}''$$

$$+ \frac{1}{V^2} \int w(\boldsymbol{x})^2\, n(\boldsymbol{x})\, \mathrm{e}^{\mathrm{i}(k-k').x}\, \mathrm{d}^3 \boldsymbol{x}, \tag{A22}$$

where for clarity we have dropped the angled brackets in the symbols n and n_w in this and all subsequent equations. If $P(\boldsymbol{k})$ varies sufficiently slowly compared to the width of $\tilde{n}_w(\delta\boldsymbol{k})$, we can approximate the first term as

$$\frac{1}{(2\pi)^3}\, P(\boldsymbol{k}) \int \tilde{n}_w(\boldsymbol{k} - \boldsymbol{k}'')\, \tilde{n}_w^*(\boldsymbol{k}' - \boldsymbol{k}'')\, \mathrm{d}^3 \boldsymbol{k}'' \tag{A23}$$

where writing $\tilde{n}_w(\boldsymbol{k}) = (1/V) \int n_w(\boldsymbol{x})\, \mathrm{e}^{\mathrm{i}k.x}\, \mathrm{d}^3 \boldsymbol{x}$ we find that

$$\int \tilde{n}_w(\boldsymbol{k} - \boldsymbol{k}'')\, \tilde{n}_w^*(\boldsymbol{k}' - \boldsymbol{k}'')\, \mathrm{d}^3 \boldsymbol{k}''$$

$$= \frac{(2\pi)^3}{V^2} \int n_w^2(\boldsymbol{x})\, \mathrm{e}^{\mathrm{i}(k-k').x}\, \mathrm{d}^3 \boldsymbol{x}. \tag{A24}$$

Hence, we derive the final expression

$$\langle \tilde{\delta}(\boldsymbol{k})\, \tilde{\delta}^*(\boldsymbol{k}')\rangle \approx \frac{1}{V} \left[P(\boldsymbol{k})\, \tilde{Q}(\boldsymbol{k} - \boldsymbol{k}') + \tilde{S}(\boldsymbol{k} - \boldsymbol{k}') \right] \tag{A25}$$

in terms of

$$Q(\boldsymbol{x}) = n_w^2(\boldsymbol{x}) \equiv n^2(\boldsymbol{x})\, w^2(\boldsymbol{x}) \tag{A26}$$

$$S(\boldsymbol{x}) = n(\boldsymbol{x})\, w^2(\boldsymbol{x}). \tag{A27}$$

Considering the special case $\boldsymbol{k}' = \boldsymbol{k}$, we see that an estimator for the auto-power spectrum is

$$\hat{P}(\boldsymbol{k}) = \frac{V\, |\tilde{\delta}(\boldsymbol{k})|^2 - \tilde{S}(0)}{\tilde{Q}(0)} \tag{A28}$$

such that

$$\langle \hat{P}(\boldsymbol{k})\rangle = \frac{V\, \langle |\tilde{\delta}(\boldsymbol{k})|^2\rangle - \tilde{S}(0)}{\tilde{Q}(0)} \approx P(\boldsymbol{k}), \tag{A29}$$

where we note that the exact expression is the convolution

$$\langle \hat{P}(\boldsymbol{k})\rangle = \frac{V^3}{(2\pi)^3} \int P(\boldsymbol{k}')\, |\tilde{n}_w(\boldsymbol{k} - \boldsymbol{k}')|^2\, \mathrm{d}^3 \boldsymbol{k}'. \tag{A30}$$

We note the special case of a constant selection function $n(\boldsymbol{x}) = n_0 = N/V$ and weights $w(\boldsymbol{x}) = 1$. In this case, $Q = N^2/V^2$ and $S = N/V$, such that

$$\hat{P}(\boldsymbol{k}) = V \left[\frac{V^2\, |\tilde{\delta}(\boldsymbol{k})|^2 - N}{N^2} \right]. \tag{A31}$$

Converting these relations to an FFT-based estimator, we grid the galaxy number distribution into the FFT cells and write this number distribution as $N(\boldsymbol{x})$. Imposing the normalization that $\sum_{\boldsymbol{x}} N(\boldsymbol{x}) = N$, we find that $N(\boldsymbol{x}) = (V/N_c)\, n(\boldsymbol{x})$. We define the selection function grid as $W(\boldsymbol{x})$, adopting the normalization convention that $\sum_{\boldsymbol{x}} W(\boldsymbol{x}) = 1$. In this case, $W(\boldsymbol{x}) = (V/N_c N)\langle n(\boldsymbol{x})\rangle$. Writing $N_w(\boldsymbol{x}) = w(\boldsymbol{x})\, N(\boldsymbol{x})$ and $W_w(\boldsymbol{x}) = w(\boldsymbol{x})\, W(\boldsymbol{x})$, we have

$$\tilde{\delta}(\boldsymbol{k}) = \frac{1}{V} \left[\tilde{N}_w - N\, \tilde{W}_w \right], \tag{A32}$$

where $\tilde{N}_w \equiv \mathrm{FFT}(N_w)$ and $\tilde{W}_w \equiv \mathrm{FFT}(W_w)$. The power-spectrum estimator becomes

$$\hat{P}(\boldsymbol{k}) = V \left[\frac{|\tilde{N}_w - N\, \tilde{W}_w|^2 - N \sum W(\boldsymbol{x}) w(\boldsymbol{x})^2}{N_c\, N^2 \sum W(\boldsymbol{x})^2\, w(\boldsymbol{x})^2} \right]. \tag{A33}$$

A3 Estimator for the cross-power spectrum

The development of the cross-power spectrum estimator follows a similar course, where we consider the two galaxy overdensity fields

$$\delta_1(\boldsymbol{x}) = w_1(\boldsymbol{x}) \left[n_1(\boldsymbol{x}) - \langle n_1(\boldsymbol{x})\rangle \right] \tag{A34}$$

$$\delta_2(\boldsymbol{x}) = w_2(\boldsymbol{x}) \left[n_2(\boldsymbol{x}) - \langle n_2(\boldsymbol{x})\rangle \right]. \tag{A35}$$

The generalization of equation (A17) is

$$\langle \tilde{\delta}_1(\boldsymbol{k})\, \tilde{\delta}_2^*(\boldsymbol{k}')\rangle = \frac{1}{V^2} \sum_{i,j} w_{1,i}\, w_{2,j} \left(\langle N_{1,i}\, N_{2,j}\rangle \right.$$

$$\left. - \langle N_{1,i}\rangle\langle N_{2,j}\rangle \right) \mathrm{e}^{\mathrm{i}(k.x_i - k'.x_j)}. \tag{A36}$$

The terms with $j = i$ now vanish, and the equivalent of equations (A19) and (A21) now involves the cross-correlation function $\xi_c(\boldsymbol{x}, \boldsymbol{x}')$ and cross-power spectrum $P_c(\boldsymbol{k})$. We obtain

$$\langle \tilde{\delta}_1(\boldsymbol{k})\, \tilde{\delta}_2^*(\boldsymbol{k}')\rangle$$

$$= \frac{1}{(2\pi)^3} \int P_c(\boldsymbol{k}'')\, \tilde{n}_{w,1}(\boldsymbol{k} - \boldsymbol{k}'')\, \tilde{n}_{w,2}^*(\boldsymbol{k}' - \boldsymbol{k}'')\, \mathrm{d}^3 \boldsymbol{k}'' \tag{A37}$$

with the approximation, which again holds if $P_c(\boldsymbol{k})$ varies sufficiently slowly compared to the width of $\tilde{n}_{w,\alpha}(\delta\boldsymbol{k})$,

$$\langle \tilde{\delta}_1(\boldsymbol{k})\, \tilde{\delta}_2^*(\boldsymbol{k}')\rangle \approx \frac{P_c(\boldsymbol{k})}{V^2} \int n_{w,1}(\boldsymbol{x})\, n_{w,2}(\boldsymbol{x})\, \mathrm{e}^{\mathrm{i}(k-k').x}\, \mathrm{d}^3 \boldsymbol{x}. \tag{A38}$$

We define

$$Q_c(\boldsymbol{x}) = n_{w,1}(\boldsymbol{x})\, n_{w,2}(\boldsymbol{x}) = w_1(\boldsymbol{x})\, n_1(\boldsymbol{x})\, w_2(\boldsymbol{x})\, n_2(\boldsymbol{x}) \tag{A39}$$

such that

$$\langle \tilde{\delta}_1(\boldsymbol{k})\, \tilde{\delta}_2^*(\boldsymbol{k}')\rangle \approx \frac{1}{V}\, P_c(\boldsymbol{k})\, \tilde{Q}_c(\boldsymbol{k} - \boldsymbol{k}'). \tag{A40}$$

The estimator for the cross-power spectrum is then written as

$$\hat{P}_c(\boldsymbol{k}) = \frac{V\, \mathrm{Re}\left\{ \tilde{\delta}_1(\boldsymbol{k})\, \tilde{\delta}_2^*(\boldsymbol{k}) \right\}}{\tilde{Q}_c(0)}$$

$$= \frac{V \left[\tilde{\delta}_1(\boldsymbol{k})\, \tilde{\delta}_2^*(\boldsymbol{k}) + \tilde{\delta}_1^*(\boldsymbol{k})\, \tilde{\delta}_2(\boldsymbol{k}) \right]}{2\, \tilde{Q}_c(0)} \tag{A41}$$

such that it is symmetric in the two indices, and

$$\langle \hat{P}_c(\boldsymbol{k})\rangle = \frac{V \left[\langle \tilde{\delta}_1(\boldsymbol{k})\, \tilde{\delta}_2^*(\boldsymbol{k})\rangle + \langle \tilde{\delta}_1^*(\boldsymbol{k})\, \tilde{\delta}_2(\boldsymbol{k})\rangle \right]}{2\, \tilde{Q}_c(0)} \approx P_c(\boldsymbol{k}) \tag{A42}$$

with the exact expression

$$\langle \hat{P}_c(\boldsymbol{k})\rangle = \frac{V^3}{(2\pi)^3} \int P_c(\boldsymbol{k}'')\, \tilde{n}_{w,1}(\boldsymbol{k} - \boldsymbol{k}'')\, \tilde{n}_{w,2}^*(\boldsymbol{k}' - \boldsymbol{k}'')\, \mathrm{d}^3 \boldsymbol{k}''. \tag{A43}$$

The FFT-based estimator is

$$\hat{P}_c(\mathbf{k}) = \frac{V \, \mathrm{Re}\{[\tilde{N}_{w,1} - N_1 \, \tilde{W}_{w,1}][\tilde{N}_{w,2} - N_2 \, \tilde{W}_{w,2}]^*\}}{N_c \, N_1 \, N_2 \, \sum W_1(\mathbf{x}) \, w_1(\mathbf{x}) \, W_2(\mathbf{x}) \, w_2(\mathbf{x})}. \tag{A44}$$

A4 Covariance between estimators

We now consider the covariance between the estimators for the auto-power spectra of the two galaxy populations, $\hat{P}_1$ and $\hat{P}_2$, and the estimator for the cross-power spectrum $\hat{P}_c$. Defining $\delta\hat{P}(\mathbf{k}) \equiv \hat{P}(\mathbf{k}) - \langle\hat{P}(\mathbf{k})\rangle$, these covariances can be written as

$$\langle \delta\hat{P}_1(\mathbf{k}) \, \delta\hat{P}_1(\mathbf{k}') \rangle = \frac{V^2 \, \langle \tilde{\delta}_1(\mathbf{k}) \, \tilde{\delta}_1^*(\mathbf{k}) \, \tilde{\delta}_1(\mathbf{k}') \, \tilde{\delta}_1^*(\mathbf{k}') \rangle}{\tilde{Q}_1(0)^2} \tag{A45}$$

$$\langle \delta\hat{P}_1(\mathbf{k}) \, \delta\hat{P}_2(\mathbf{k}') \rangle = \frac{V^2 \, \langle \tilde{\delta}_1(\mathbf{k}) \, \tilde{\delta}_1^*(\mathbf{k}) \, \tilde{\delta}_2(\mathbf{k}') \, \tilde{\delta}_2^*(\mathbf{k}') \rangle}{\tilde{Q}_1(0) \, \tilde{Q}_2(0)} \tag{A46}$$

$$\langle \delta\hat{P}_1(\mathbf{k}) \, \delta\hat{P}_c(\mathbf{k}') \rangle = \frac{V^2}{2 \, \tilde{Q}_1(0) \, \tilde{Q}_c(0)}$$
$$\times \, \left[\langle \tilde{\delta}_1(\mathbf{k}) \, \tilde{\delta}_1^*(\mathbf{k}) \, \tilde{\delta}_1(\mathbf{k}') \, \tilde{\delta}_2^*(\mathbf{k}') \rangle \right.$$
$$+ \, \left. \langle \tilde{\delta}_1(\mathbf{k}) \, \tilde{\delta}_1^*(\mathbf{k}) \, \tilde{\delta}_1^*(\mathbf{k}') \, \tilde{\delta}_2(\mathbf{k}') \rangle \right] \tag{A47}$$

$$\langle \delta\hat{P}_c(\mathbf{k}) \, \delta\hat{P}_c(\mathbf{k}') \rangle = \frac{V^2}{4 \, \tilde{Q}_c(0)^2}$$
$$\times \, \left[\langle \tilde{\delta}_1(\mathbf{k}) \, \tilde{\delta}_2^*(\mathbf{k}) \, \tilde{\delta}_1(\mathbf{k}') \, \tilde{\delta}_2^*(\mathbf{k}') \rangle \right.$$
$$+ \, \langle \tilde{\delta}_1(\mathbf{k}) \, \tilde{\delta}_2^*(\mathbf{k}) \, \tilde{\delta}_1^*(\mathbf{k}') \, \tilde{\delta}_2(\mathbf{k}') \rangle$$
$$+ \, \langle \tilde{\delta}_1^*(\mathbf{k}) \, \tilde{\delta}_2(\mathbf{k}) \, \tilde{\delta}_1(\mathbf{k}') \, \tilde{\delta}_2^*(\mathbf{k}') \rangle$$
$$+ \, \left. \langle \tilde{\delta}_1^*(\mathbf{k}) \, \tilde{\delta}_2(\mathbf{k}) \, \tilde{\delta}_1^*(\mathbf{k}') \, \tilde{\delta}_2(\mathbf{k}') \rangle \right]. \tag{A48}$$

Taking the first expression as an example, these relations may be evaluated by substituting $\tilde{\delta}(\mathbf{k}) = \sum_{\mathbf{x}} \delta(\mathbf{x}) \, \mathrm{e}^{i\mathbf{k}\cdot\mathbf{x}}$. We can then write the product $\langle \tilde{\delta}(\mathbf{k}) \, \tilde{\delta}^*(\mathbf{k}) \, \tilde{\delta}(\mathbf{k}') \, \tilde{\delta}^*(\mathbf{k}') \rangle$ as

$$\sum_{\mathbf{x}_1, \mathbf{x}_2, \mathbf{x}_3, \mathbf{x}_4} \langle \delta(\mathbf{x}_1)\delta(\mathbf{x}_2)\delta(\mathbf{x}_3)\delta(\mathbf{x}_4) \rangle \, \mathrm{e}^{i[\mathbf{k}\cdot(\mathbf{x}_1-\mathbf{x}_2)+\mathbf{k}'\cdot(\mathbf{x}_3-\mathbf{x}_4)]}. \tag{A49}$$

Expectation values of individual terms in the product satisfy $\langle \delta(\mathbf{x}) \rangle = 0$; non-zero terms are those in which the indices of the sum satisfy $(1 = 2, 3 = 4)$, $(1 = 3, 2 = 4)$ or $(1 = 4, 2 = 3)$. Splitting the sum into these combinations, it can be expressed as

$$\sum_{\mathbf{x}, \mathbf{x}'} \{ \langle \delta(\mathbf{x})\delta(\mathbf{x}) \rangle \langle \delta(\mathbf{x}')\delta(\mathbf{x}') \rangle$$

$$+ \, \langle \delta(\mathbf{x})\delta(\mathbf{x}) \rangle \langle \delta(\mathbf{x}')\delta(\mathbf{x}') \rangle \, \mathrm{e}^{i(\mathbf{k}-\mathbf{k}')\cdot(\mathbf{x}-\mathbf{x}')}$$

$$+ \, \langle \delta(\mathbf{x})\delta(\mathbf{x}) \rangle \langle \delta(\mathbf{x}')\delta(\mathbf{x}') \rangle \, \mathrm{e}^{i(\mathbf{k}+\mathbf{k}')\cdot(\mathbf{x}-\mathbf{x}')} \}. \tag{A50}$$

We obtain

$$\langle \delta\hat{P}_1(\mathbf{k}) \, \delta\hat{P}_1(\mathbf{k}') \rangle = \frac{V^2 \, |\langle \tilde{\delta}_1(\mathbf{k}) \, \tilde{\delta}_1^*(\mathbf{k}') \rangle|^2}{\tilde{Q}_1(0)^2} \tag{A51}$$

$$\langle \delta\hat{P}_1(\mathbf{k}) \, \delta\hat{P}_2(\mathbf{k}') \rangle = \frac{V^2 \, |\langle \tilde{\delta}_1(\mathbf{k}) \, \tilde{\delta}_2^*(\mathbf{k}') \rangle|^2}{\tilde{Q}_1(0) \, \tilde{Q}_2(0)} \tag{A52}$$

$$\langle \delta\hat{P}_1(\mathbf{k}) \, \delta\hat{P}_c(\mathbf{k}') \rangle = \frac{V^2 \, \mathrm{Re} \left\{ \langle \tilde{\delta}_1(\mathbf{k}) \, \tilde{\delta}_1^*(\mathbf{k}') \rangle \, \langle \tilde{\delta}_1(\mathbf{k}) \, \tilde{\delta}_2^*(\vec{k}') \rangle \right\}}{\tilde{Q}_1(0) \, \tilde{Q}_c(0)} \tag{A53}$$

$$\langle \delta\hat{P}_c(\mathbf{k}) \, \delta\hat{P}_c(\mathbf{k}') \rangle = \frac{V^2}{2 \, \tilde{Q}_c(0)^2} \left\{ |\langle \tilde{\delta}_1(\mathbf{k}) \, \tilde{\delta}_2^*(\mathbf{k}') \rangle|^2 \right.$$
$$+ \, \left. \mathrm{Re} \left\{ \langle \tilde{\delta}_1(\mathbf{k}) \, \tilde{\delta}_1(\mathbf{k}') \rangle \langle \tilde{\delta}_2(\mathbf{k}) \, \tilde{\delta}_2(\mathbf{k}') \rangle \right\} \right\}. \tag{A54}$$

Writing $\delta\mathbf{k} = \mathbf{k} - \mathbf{k}'$ and using the approximate relations in equations (A25) and (A40) gives

$$\langle \delta\hat{P}_1(\mathbf{k}) \, \delta\hat{P}_1(\mathbf{k}') \rangle = \frac{|P_1(\mathbf{k}) \, \tilde{Q}_1(\delta\mathbf{k}) + \tilde{S}_1(\delta\mathbf{k})|^2}{\tilde{Q}_1(0)^2} \tag{A55}$$

$$\langle \delta\hat{P}_1(\mathbf{k}) \, \delta\hat{P}_2(\mathbf{k}') \rangle = \frac{|P_c(\mathbf{k}) \, \tilde{Q}_c(\delta\mathbf{k})|^2}{\tilde{Q}_1(0) \, \tilde{Q}_2(0)} \tag{A56}$$

$$\langle \delta\hat{P}_1(\mathbf{k}) \, \delta\hat{P}_c(\mathbf{k}') \rangle = \frac{\mathrm{Re} \left\{ \left[P_1(\mathbf{k}) \, \tilde{Q}_1(\delta\mathbf{k}) + \tilde{S}_1(\delta\mathbf{k}) \right] \, P_c(\mathbf{k}) \, Q_c^*(\delta\mathbf{k}) \right\}}{\tilde{Q}_1(0) \, \tilde{Q}_c(0)} \tag{A57}$$

$$\langle \delta\hat{P}_c(\mathbf{k}) \, \delta\hat{P}_c(\mathbf{k}') \rangle = \frac{1}{2 \, \tilde{Q}_c(0)^2} |P_c(\mathbf{k}) \, \tilde{Q}_c(\delta\mathbf{k})|^2$$
$$+ \, \mathrm{Re} \left\{ \left[P_1(\mathbf{k}) \, \tilde{Q}_1(\delta\mathbf{k}) + \tilde{S}_1(\delta\mathbf{k}) \right] \, \left[P_2(\mathbf{k}) \, \tilde{Q}_2(\delta\mathbf{k}) + \tilde{S}_2(\delta\mathbf{k}) \right]^* \right\}. \tag{A58}$$

For a uniform selection function, the equations simplify to

$$\langle \delta\hat{P}_1 \, \delta\hat{P}_1 \rangle = \left(P_1 + \frac{1}{n_1} \right)^2 \tag{A59}$$

$$\langle \delta\hat{P}_1 \, \delta\hat{P}_2 \rangle = P_c^2 \tag{A60}$$

$$\langle \delta\hat{P}_1 \, \delta\hat{P}_c \rangle = P_c \left(P_1 + \frac{1}{n_1} \right) \tag{A61}$$

$$\langle \delta\hat{P}_c \, \delta\hat{P}_c \rangle = \frac{1}{2} \left[P_c^2 + \left(P_1 + \frac{1}{n_1} \right) \left(P_2 + \frac{1}{n_2} \right) \right], \tag{A62}$$

where $n_1 = N_1/V$ and $n_2 = N_2/V$.

This paper has been typeset from a TeX/LaTeX file prepared by the author.